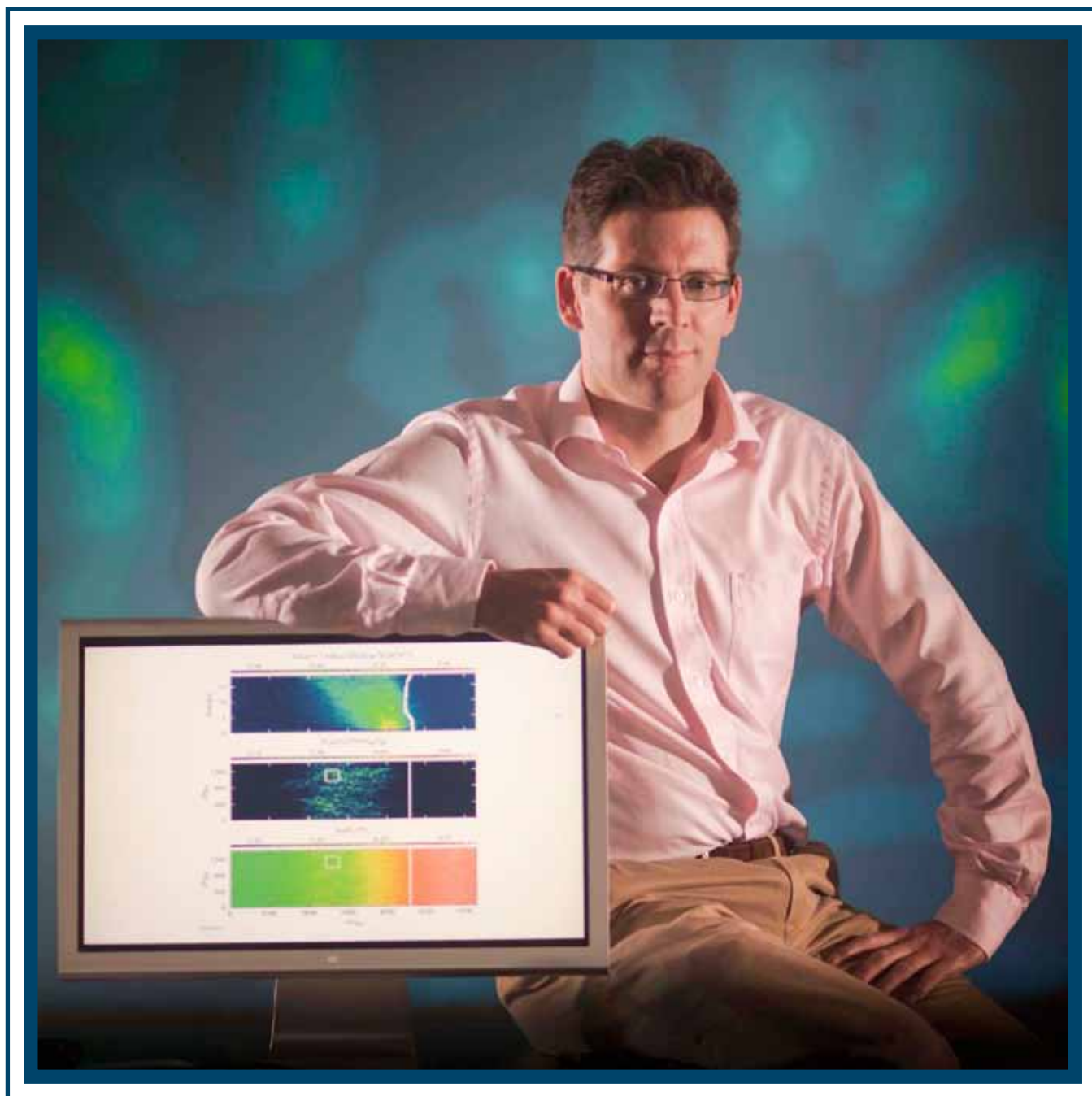


LLE Review

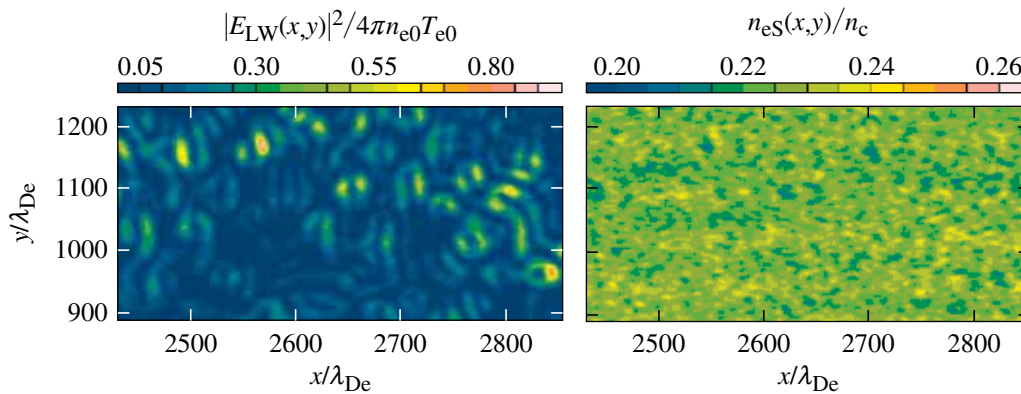
Quarterly Report



About the Cover:

The cover photo shows Dr. Jason Myatt presenting simulation results that describe Langmuir turbulence and suprathermal electron production from the two-plasmon-decay instability driven by crossed laser beams in inhomogeneous plasma. In the foreground are plots of the caviton correlator, Langmuir wave energy density, and the low-frequency density fluctuation. The solid curve on the top panel represents the spatiotemporal evolution of the quarter-critical surface. The boxes in the middle and bottom panels mark regions where Langmuir cavitation and collapse are examined in greater spatial detail.

The image below shows the magnified spatial region where caviton activity is observed. Several stages of nucleation and collapse are observed simultaneously.



This report was prepared as an account of work conducted by the Laboratory for Laser Energetics and sponsored by New York State Energy Research and Development Authority, the University of Rochester, the U.S. Department of Energy, and other agencies. Neither the above named sponsors, nor any of their employees, makes any warranty, expressed or implied, or assumes any legal liability or responsibility for the accuracy, completeness, or usefulness of any information, apparatus, product, or process disclosed, or represents that its use would not infringe privately owned rights. Reference herein to any specific commercial product, process, or service by trade name, mark, manufacturer, or otherwise, does not necessarily constitute or imply its endorsement, recommendation, or favoring

by the United States Government or any agency thereof or any other sponsor. Results reported in the LLE Review should not be taken as necessarily final results as they represent active research. The views and opinions of authors expressed herein do not necessarily state or reflect those of any of the above sponsoring entities.

The work described in this volume includes current research at the Laboratory for Laser Energetics, which is supported by New York State Energy Research and Development Authority, the University of Rochester, the U.S. Department of Energy Office of Inertial Confinement Fusion under Cooperative Agreement No. DE-FC52-08NA28302, and other agencies.

Printed in the United States of America

Available from

National Technical Information Services

U.S. Department of Commerce

5285 Port Royal Road

Springfield, VA 22161

www.ntis.gov

For questions or comments, contact Philip M. Nilson, Editor, Laboratory for Laser Energetics, 250 East River Road, Rochester, NY 14623-1299, (585) 275-9527.

Worldwide-Web Home Page: <http://www.lle.rochester.edu/>
(Color online)

LLE Review

Quarterly Report



Contents

In Brief	iii
Langmuir Turbulence and Suprathermal Electron Production from the Two-Plasmon-Decay Instability Driven by Crossed Laser Beams in an Inhomogeneous Plasma	109
Demonstration of a Closed-Loop Beam-Shaping System Based on the Phase-Only Carrier Method in High-Power Lasers	113
Temporal Contrast Degradation at the Focus of Ultrafast Pulses from High-Frequency Spectral Phase Modulation	117
Highly Accurate Wavefront Reconstruction Algorithms Over Broad Spatial-Frequency Bandwidth	130
Time-Resolved Optical Response of All-Oxide, $\text{YBa}_2\text{Cu}_3\text{O}_7/\text{La}_{0.7}\text{Sr}_{0.3}\text{MnO}_3$ Proximitized Bilayers	141
Publications and Conference Presentations	

In Brief

This volume of the LLE Review, covering April–June 2011, features “Langmuir Turbulence and Suprathermal Electron Production from the Two-Plasmon-Decay Instability Driven by Crossed Laser Beams in an Inhomogeneous Plasma” by H. X. Vu (University of California–San Diego), D. F. DuBois (Lodestar Research Corporation and LANL), J. F. Myatt (LLE), and D. A. Russell (Lodestar Research Corporation). In this article (p. 109), the fully kinetic reduced particle-in-cell method, utilizing novel diagnostics, has been applied to simulations of the two-plasmon-decay (TPD) instability in inhomogeneous plasma for parameters consistent with recent direct-drive experiments. The nonlinear saturated state of TPD is one of Langmuir turbulence involving the coexistence of the Langmuir cavitation and collapse, the Langmuir decay instability, and ponderomotive density-profile modification. The saturated state is characterized by very spiky electric fields, and Langmuir cavitation occurs preferentially inside density channels produced by the ponderomotive beating of the crossed laser beams. Statistical analyses show that cavitons follow Gaussian statistics. At times exceeding 10 ps, the excited Langmuir turbulence moves away from the quarter-critical surface to lower densities. The heated electron-distribution function is, in all cases, bi-Maxwellian, with hot-electron temperatures in the range of 60 keV to 100 keV. In all cases considered, Langmuir cavitation and collapse provide dissipation by producing suprathermal electrons that stabilize the system in saturation and drive the Langmuir wave spectrum to the small dissipation scales at the Landau cutoff. The net hot-electron energy flux out of the system is a small fraction ($\sim 0.5\%$ to 2%) of the input laser power in these simulations.

Additional highlights of research presented in this issue include the following:

- S.-W. Bahk, E. Fess, M. Barczys, I. A. Begishev, R. K. Jungquist, M. Spilatro, and J. D. Zuegel (LLE) demonstrate the use of a closed-loop, high-resolution beam-shaping system based on a liquid-crystal-on-silicon (LCOS) spatial-light modulator (SLM) in a multiterawatt laser system and in the OMEGA EP long-pulse front end (p. 113). The closed-loop algorithm is based on the linearity of image transformation between the control device and the measured image, where miscalibration of the linear parameters or blurring of the image affects the stability of the algorithm. One of the main causes of blurring is ascribed to the presence of tilted plates and wedges in the imaging system. These are common elements in complex laser systems. Such effects can be either compensated for or avoided by careful design. The procedure and results of damage-threshold measurement for LCOS-SLM are presented to help determine a safe operation regime for this device in high-power laser systems.
- J. Bromage, C. Dorrer, and R. K. Jungquist (LLE) evaluate the impact of high-frequency spectral phase modulation on the temporal contrast of ultrafast pulses (p. 117). Expressions are derived for the low-intensity pedestal produced by optical component surface roughness within pulse stretchers and compressors. Phase noise, added across the near field of a spectrally dispersed beam, produces space–time coupling in the far field or focal plane. The pedestal is swept across an area in the focal plane many times the size of the diffraction-limited spot. Simulations are performed for generic stretchers and compressors that show fundamentally different forms of temporal contrast degradation at focus.
- S.-W. Bahk (LLE) has developed new wavefront reconstruction algorithms for high-spatial-resolution applications (p. 130). Analyzing wavefront reconstructors in the frequency domain lends new insight into ways to improve frequency response and to understand noise propagation. The mathematical tools required to analyze the frequency domain are first developed for discrete band-limited signals. These tools are shown to improve frequency response in either spatial- or frequency-domain reconstruc-

tion algorithms. A new spatial-domain iterative reconstruction algorithm based on the Simpson rule is presented. The previously developed rectangular-geometry band-limited algorithm in frequency domain is adapted to hexagonal geometry, which adds flexibility when applying frequency-domain algorithms. Finally, a generalized analytic error propagation formula is found for different types of reconstructors and compared with numerical simulations.

- L. Parlato, R. Arpaia, C. De Lisio, F. Miletto Granozio, G. Pepe, V. Pagliarulo, U. Scotti di Uccio (CNR-SPIN and Dipartimento di Scienze Fisiche, Complesso Universitario di Monte Sant' Angelo, Italy); P. Perna (IMDEA-Nanociencia, Campus Universidad Autónoma de Madrid, Spain); M. Radovic (Swiss Light Source, Switzerland); and R. Sobolewski (LLE) present femtosecond pump-probe spectroscopy studies of time-resolved optical reflectivity of all-oxide, $\text{YBa}_2\text{Cu}_3\text{O}_7/\text{La}_{0.7}\text{Sr}_{0.3}\text{MnO}_3$ superconductor/ferromagnet nano-bilayers (p. 141). The temperature dependence of the nonequilibrium carrier dynamics is investigated down to 4 K. The photoresponse of bilayers has two characteristic relaxation times that are shorter than that of the $\text{YBa}_2\text{Cu}_3\text{O}_7$ film and their superconducting properties are revealed in sharp peaks near the superconducting transition. The bilayer dynamics cannot be interpreted as an incoherent sum of contributions from the two layers; instead, the results point to an active role of an interface layer, where the electronic charge transfer from $\text{La}_{0.7}\text{Sr}_{0.3}\text{MnO}_3$ to $\text{YBa}_2\text{Cu}_3\text{O}_7$ takes place.

Philip M. Nilson
Editor

Langmuir Turbulence and Suprathermal Electron Production from the Two-Plasmon-Decay Instability Driven by Crossed Laser Beams in an Inhomogeneous Plasma

It is currently a time of great anticipation for inertial confinement fusion (ICF) research. An attempt to demonstrate ignition will likely be made at the National Ignition Facility (NIF) within the year.¹ Ignition will be attempted first in indirect-drive geometry (where the laser energy is first converted to soft x rays that drive the target), with an attempt in direct-drive geometry (where the laser directly illuminates the target) likely to occur later. In both approaches, uncertainties with regard to laser-plasma instabilities remain a serious concern. This article presents new results regarding two-plasmon-decay (TPD) instability, which is perhaps the most-serious instability for direct-drive ICF targets. TPD instability is the decay of a laser photon into two Langmuir waves (plasmons). The plasma turbulence driven by TPD produces suprathermal electrons, which can preheat the target, reducing its compressibility and negatively impacting performance.^{2–4} While TPD instability has been unambiguously observed in recent direct-drive experiments (at LLE’s OMEGA Laser Facility), in which diagnostic evidence includes the simultaneous observation of odd half-harmonic radiation and hard x rays attributable to hot-electron generation,⁵ it is not currently possible to test at the NIF scale. This makes the calculation of hot-electron generation by TPD in relevant parameter regimes highly valuable.

In previous papers, we have studied two nonlinear models of TPD in regimes relevant to the LLE experiments: (1) the extended Zakharov model (ZAK)—a reduced fluid-like model with no nonlinear kinetic effects,^{6–8} and (2) the fully kinetic reduced-description particle-in-cell (RPIC) model.⁹ It is noted here that the ZAK model has been derived directly from the RPIC model as a limiting case, primarily for weak laser drives.⁹ The significant nonlinear processes, noted in Ref. 9, included Langmuir decay instability (LDI), wherein the TPD Langmuir waves (LW’s) parametrically decay into another LW and an ion-acoustic wave (IAW). The RPIC simulations in Ref. 9 showed significant kinetic effects, such as hot-electron generation by the excited Langmuir turbulence.

This article presents new results concerning TPD instability having three key novel components. First, TPD is excited by

overlapped (crossed) laser beams, which is a generic and important feature of directly driven ICF.^{9,10} Second, it includes the effects of plasma inhomogeneity. Finally, the TPD-generated flux of suprathermal electrons and their energy spectrum are explicitly computed (tolerable levels of preheat in direct-drive designs at the NIF scale are at a level of 400 J). Included in the results is a detailed description of the structure of the nonlinear state of LW turbulence that will facilitate the construction of further-reduced models. These results have been made possible by extending the RPIC model⁹ to include these effects. The Zakharov model applied to inhomogeneous plasmas^{7,11} predicted, in addition to nonlinear effects mentioned above,^{6–8} significant electron-density profile modification caused by the ponderomotive pressure of the LW’s; this modification moved the ensuing turbulent region from densities near $n_c/4$ [$n_c = m_e \omega_0^2 / (4\pi e^2)$ is the critical density] to densities that were sufficiently low enough to stabilize TPD by Landau damping (the so-called Landau cutoff). This profile modification occurs on an ion-acoustic time scale and requires integration times of several tens of picoseconds (ps). The identification of the primary TPD LW’s and secondary nonlinear fluctuations, such as those caused by LDI, involves the Fourier spectra of the LW envelope and low-frequency electron-density fields, similar to the procedure in Ref. 9, and will be demonstrated elsewhere.¹²

For all of the two-dimensional (2-D) simulations considered here, the plasma consisted of a linear gradient with electron density n_e/n_c varying from 0.19 to 0.27 over an axial (x) extent of 45 μm , resulting in a gradient scale length $L_n \approx 130 \mu\text{m}$. The transverse (y) extent of the plasma was 10 μm and the temperatures $T_{e0} = 2 \text{ keV}$ and $T_{i0} = 1 \text{ keV}$. The incident pump laser light consisted of spatially uniform plane waves propagating at angles $\pm 23^\circ$ with respect to the x axis, each with a fluence of I_0 and wavelength $\lambda_0 = 351 \text{ nm}$, with polarizations in the x - y plane. The linear density gradient under consideration was compatible with the frequency envelope representation of the LW fields because the electron-plasma frequency varied by $\sim \pm 4\%$ about the reference envelope frequency, chosen to be in the center of the simulation domain for which $n_e/n_c = 0.23$. The linear energy growth rate γ versus (beamlet) fluence I_0 was

obtained from a series of RPIC simulations in which only I_0 was varied. A very good fit to these data is given by the best-fit empirical expression $\gamma(I_0) = \gamma_0(I_0/I_{\text{thres}} - 1)$, where $I_{\text{thres}} \approx 1 \times 10^{15} \text{ W/cm}^2$ and $\gamma_0 \approx 5.8 \text{ ps}^{-1}$. A more-detailed discussion of the RPIC thresholds and the influence of discrete particle effects will be given elsewhere.¹² It is observed in all of our RPIC simulations that above threshold ($I_0/I_{\text{thres}} > 1$), Langmuir cavitation and collapse are observed at very early times (comparable to the e -folding time of the linear TPD growth), even for cases just above the TPD threshold, and appear to be primarily responsible for suprathermal electron production and nonlinear saturation of TPD.

A representative RPIC simulation with $I_0/I_{\text{thres}} = 2$ is analyzed in detail to illustrate our results. To quantify whether Langmuir cavitation actually occurs, we compute the ‘‘caviton correlator’’ (Ref. 13):

$$C(x,t) = \langle -\delta n |E_{\text{LW}}|^2 \rangle_y / \left[\langle (\delta n)_y \rangle_y^{1/2} \langle |E_{\text{LW}}|^2 \rangle_y \right],$$

where the operator $\langle \rangle_y$ denotes averaging in the transverse (y) direction, δn is the low-frequency electron-density perturbation, and E_{LW} is the LW field envelope. A *caviton* is essentially a local maximum of $|E_{\text{LW}}|^2$, spatially coincident with a local minimum of δn (i.e., $\delta n < 0$). Figure 127.1 plots $C(x,t)$, $E_{\text{LW}}(x,y)$, and $\delta n(x,y)$ at $t = 20 \text{ ps}$. The solid curve on the top panel represents the spatiotemporal evolution of the quarter-critical surface. The boxes in the middle and bottom panels mark regions where Langmuir cavitation and collapse will be examined in greater spatial detail (see Fig. 127.3). As indicated in the top panel of Fig. 127.1, Langmuir cavitation and collapse are observed within a short time ($t < 1 \text{ ps}$) and are observed to be accompanied by the production of suprathermal electrons after a short delay ($\tau < 2 \text{ ps}$), leading to nonlinear saturation of TPD, while throughout this process, the IAW’s

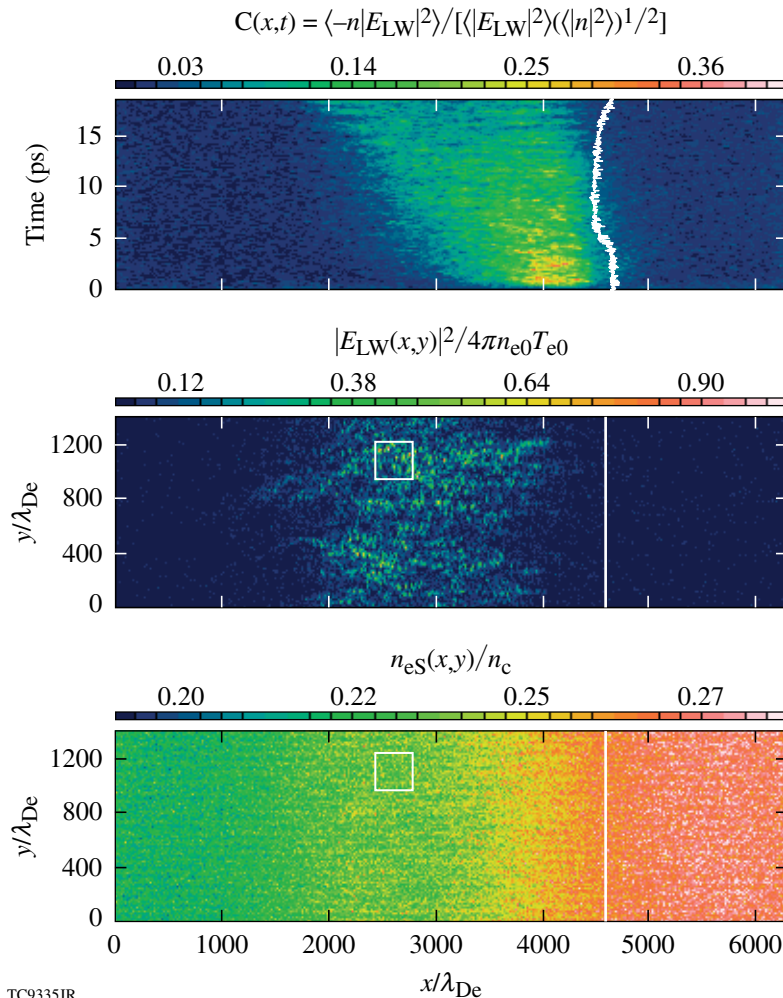


Figure 127.1

Plots of the caviton correlator $C(x,t)$, LW energy density, and the low-frequency density fluctuation at $t = 20 \text{ ps}$. The solid curve on the top panel represents the spatiotemporal evolution of the quarter-critical surface. The boxes in the middle and bottom panels mark regions where Langmuir cavitation and collapse will be examined in greater spatial detail (see Fig. 127.3). Langmuir cavitation and collapse are observed to occur for $2000 < x/\lambda_{\text{De}} < 4000$.

participating in LDI have weak Fourier spectral amplitudes. The ponderomotive beating of the obliquely propagating laser waves produces a standing-wave pattern, which manifests itself as density channels on the background plasma seen in the bottom panel of Fig. 127.1. Langmuir cavitation and collapse occur preferentially in these density channels and in sufficiently strongly driven cases, can lead to “kinking” of these initially straight channels, perhaps signaling that the channels will self-focus or filament in three-dimensional (3-D) simulations. Plots of the caviton correlation as a function of density and time (not shown) indicate that LW activity peaks at $n_e/n_c \sim 0.24$, where the forward TPD LW’s become degenerate and overlap for laser-propagation angles of $\pm 23^\circ$ and $T_{e0} = 2$ keV (Refs. 9–12). In addition to $C(x,t)$ shown in Fig. 127.1, which indicates that all Langmuir cavitation and collapse occur in the active region $2000 < x/\lambda_{De} < 4000$, one can perform a statistical analysis by defining (for the purposes of this study) a caviton as a spatial local maximum of $|E_{LW}(x,y)|^2$ that exceeds $10\times$ the average LW energy density in the active region. All local maxima identified as cavitons by this criterion are plotted as a caviton-distribution function versus the normalized LW energy density $|E_{LW}|^2/4\pi n_{e0}T_{e0}$. Interestingly, it is found that cavitons follow Gaussian statistics for all RPIC simulations under consideration at each given time. In addition, the heated-electron distribution is found to be bi-Maxwellian. As an example, caviton statistics and the heated-electron-distribution function, at $t = 13$ ps, for the simulation described in Fig. 127.1, are shown in Fig. 127.2. The average LW energy density in the active region is $\langle |E_{LW}|^2 \rangle / 4\pi n_{e0}T_{e0} \sim 0.05$, and cavitons are distributed according to $F(|E_{LW}|^2) \propto \exp(-|E_{LW}|^2/4\pi n_{e0}T_{e0}\epsilon)$, where $\epsilon \approx 0.135$. The v_y -averaged electron distribution shows a bi-Maxwellian distribution with a bulk temperature of $T_{bulk} \approx 1.1 T_{e0} = 2.2$ keV (slightly heated above T_{e0}) and a suprathermal

electron temperature $T_{hot} \approx 30 T_{e0} = 60$ keV. It is observed that T_{hot} depends on the strength of the laser drive and not on the kinetic energy associated with the phase velocity of the primary LW.

The electric-field intensity $|E(x,y)|^2$ is very spiky, with about 10^4 cavitons (by the above criterion) present in the active region at any given time after the system reaches saturation. Some of these cavitons can proceed to collapse and “burn out,” wherein all the electrostatic energy is given up to accelerated electrons. It has been argued that in 2-D, cavitons must gather a finite amount of electrostatic energy before collapse can occur, whereas in 3-D, this threshold energy is zero. In 3-D, collapse events are expected to be weaker but more numerous.¹⁴ Magnification of a spatial region where caviton activity is observed is shown in Fig. 127.3. Several stages of the nucleation–collapse–burnout caviton cycle are observed simultaneously. Frequency spectral diagnostics of the LW envelope fields were employed in corresponding ZAK simulations, which show significant LW energy for frequencies below the local electron-plasma frequency—an unambiguous signature of collapse.^{13,14} Finally, the time history of the suprathermal heat flux through simulation boundaries indicates that the simulation is slowly approaching a nonlinear saturated state with $\sim 1.5\%$ of the input laser fluence converted into suprathermal heat flux at 20 ps.

In summary, we have performed a number of RPIC simulations with varying laser fluences for the parameters listed above. Our simulations, spanning a wide range of laser fluences ($I_0/I_{thres} = 1$ to 4), indicate the following salient features, which are also qualitatively observed in Zakharov simulations¹² and quasi-linear Zakharov simulations.¹⁵ First, the ponderomotive beating of the crossed laser beams creates a standing wave

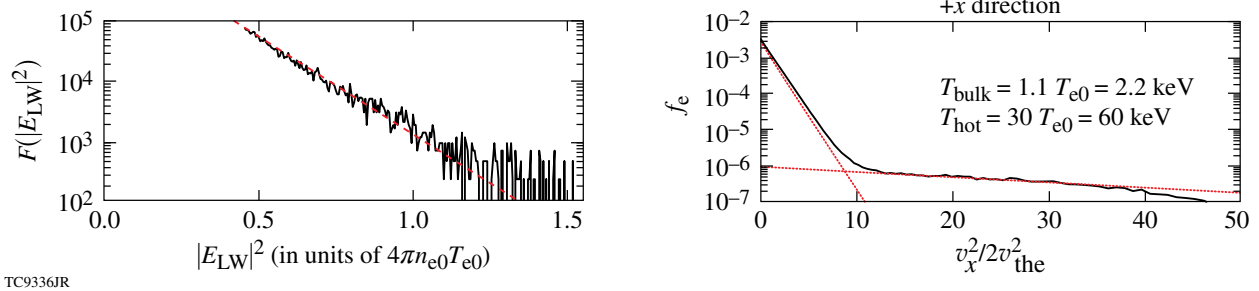
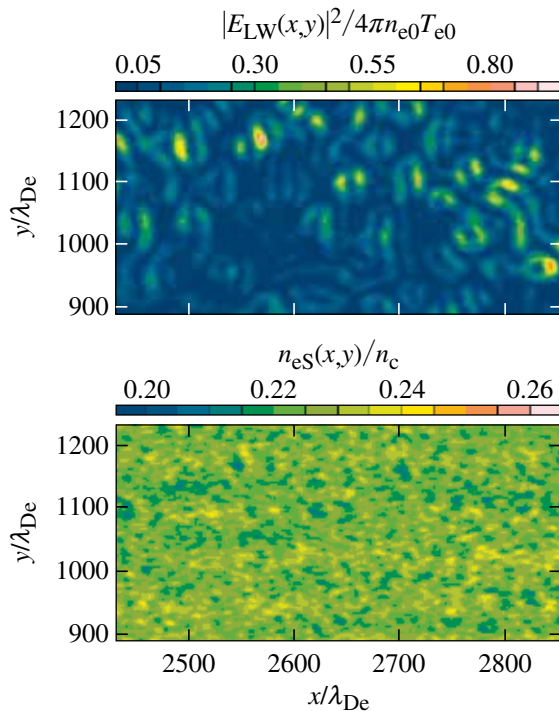


Figure 127.2

Caviton statistics and the heated-electron-distribution function at $t = 13$ ps. The spatial average LW energy density in the active region is $\langle |E_{LW}|^2 \rangle / 4\pi n_{e0}T_{e0} \sim 0.04$, and cavitons follow the distribution $F(|E_{LW}|^2) \propto \exp(-|E_{LW}|^2/4\pi n_{e0}T_{e0}\epsilon)$, where $\epsilon \approx 0.135$. The total number of cavitons $N = \int_{\epsilon_{min}}^{\infty} F(|E_{LW}|^2) d(|E_{LW}|^2)$. The v_y -averaged electron distribution shows a bi-Maxwellian distribution with a bulk temperature of $T_{bulk} \approx 1.1 T_{e0} = 2.2$ keV (slightly heated above the initial temperature) and a suprathermal electron temperature $T_{hot} \approx 30 T_{e0} = 60$ keV.



TC9337JR

Figure 127.3

Magnification of a spatial region where caviton activity is observed (marked by the boxes in the middle and bottom panels of Fig. 127.1). Several stages of nucleation and collapse are observed simultaneously.

pattern, manifested as density channels in which Langmuir cavitation and collapse preferentially occur. Second, Langmuir cavitation and collapse occur at early times ($t < 1$ ps), accompanied by suprathermal electron production and nonlinear saturation of TPD. These observations lead us to the preliminary conclusion that LDI, which is observed in the low-frequency density-fluctuation spectrum for stronger drive, plays a secondary role in the nonlinear saturation of TPD in the regimes studied here. (A more-complete understanding of the competition of cavitation, collapse, and LDI, along with their contribution to electron acceleration, warrants further study.) Third, cavitons are shown to follow Gaussian statistics, a general observation in both RPIC and ZAK simulations, regardless of drive strength (as long as the drives are sufficiently strong to cause Langmuir cavitation). The suprathermal electron-distribution function is observed in all cases to be bi-Maxwellian, with hot temperatures reaching 60 to 100 keV in our simulations. The suprathermal heat flux out of the simulation domain, normalized to the overlapped laser fluence, achieved values of 0.5% to 2% for the RPIC simulations considered here. Langmuir collapse and burnout provide the dissipation (into fast electrons) that stabilizes the system in saturation and drives the LW spectrum to the small dissipation scales at the “Landau cutoff.”

ACKNOWLEDGMENT

This research was supported by the U.S. Department of Energy, Office of Inertial Confinement Fusion under Cooperative Agreement No. DE-FC52-08NA28302, the University of Rochester, and the New York State Energy Research and Development Authority, and the National Nuclear Security Agency through its High-Energy-Density Laboratory Plasmas Grant No. DE-FG52-09NA29545. The support of DOE does not constitute an endorsement by DOE of the views expressed in this article.

REFERENCES

1. S. H. Glenzer *et al.*, Phys. Rev. Lett. **106**, 085004 (2011).
2. J. A. Delettrez, V. N. Goncharov, P. B. Radha, C. Stoeckl, A. V. Maximov, T. C. Sangster, J. A. Frenje, and D. Shvarts, Bull. Am. Phys. Soc. **53**, 248 (2008).
3. V. A. Smalyuk, D. Shvarts, R. Betti, J. A. Delettrez, D. H. Edgell, V. Yu. Glebov, V. N. Goncharov, R. L. McCrory, D. D. Meyerhofer, P. B. Radha, S. P. Regan, T. C. Sangster, W. Seka, S. Skupsky, C. Stoeckl, B. Yaakobi, J. A. Frenje, C. K. Li, R. D. Petrasso, and F. H. Séguin, Phys. Rev. Lett. **100**, 185005 (2008).
4. B. Yaakobi, C. Stoeckl, W. Seka, J. A. Delettrez, T. C. Sangster, and D. D. Meyerhofer, Phys. Plasmas **12**, 062703 (2005).
5. W. Seka, D. H. Edgell, J. F. Myatt, A. V. Maximov, R. W. Short, V. N. Goncharov, and H. A. Baldis, Phys. Plasmas **16**, 052701 (2009).
6. D. F. DuBois, D. A. Russell, and H. A. Rose, Phys. Rev. Lett. **74**, 3983 (1995).
7. D. A. Russell and D. F. DuBois, Phys. Rev. Lett. **86**, 428 (2001).
8. D. A. Russell, D. F. DuBois, and H. X. Vu, presented at the Workshop on SRS/SBS Saturation, Livermore, CA, 2–5 April 2002.
9. H. X. Vu, D. F. DuBois, D. A. Russell, and J. F. Myatt, Phys. Plasmas **17**, 072701 (2010).
10. R. W. Short, Bull. Am. Phys. Soc. **54**, 144 (2009).
11. J. F. Myatt, J. Zhang, J. A. Delettrez, A. V. Maximov, R. W. Short, W. Seka, D. H. Edgell, D. F. DuBois, D. A. Russell, and H. X. Vu, “The Dynamics of Hot-Electron Heating in Direct-Drive Implosion Experiments Due to the Two-Plasmon-Decay Instability,” submitted to Physics of Plasmas.
12. H. X. Vu, D. F. DuBois, J. F. Myatt, and D. A. Russell, “Kinetic Simulations of the Nonlinear Evolution of the Two-Plasmon-Decay Instability in an Inhomogeneous Plasma,” to be submitted to Physics of Plasmas.
13. D. F. DuBois, H. A. Rose, and D. A. Russell, Phys. Scr. **T63**, 16 (1996).
14. D. F. Dubois *et al.*, J. Geophys. Res. **98**, 17,543 (1993).
15. K. Y. Sanbonmatsu *et al.*, Phys. Plasmas **7**, 2824 (2000) and references therein.

Demonstration of a Closed-Loop Beam-Shaping System Based on the Phase-Only Carrier Method in High-Power Lasers

Beam-shaping applications in high-power laser systems have been presented in many different contexts such as the improvement of laser performance¹ or the manipulation of laser-target interactions.^{2,3} These applications commonly employ static apodizers or deformable mirrors. Spatial-light modulators (SLM's) are also popular beam-shaping devices. Because of their low damage threshold and small aperture, they have been used in laser front ends⁴ or inside laser cavities.⁵ The advantage of SLM beam shapers lies in programmability and high spatial resolution, allowing for extremely fine control of the laser-beam profile. This is an especially important feature for maximizing the performance of high-power lasers. Defects or damages sites in the compressor gratings⁶ or final optics assembly⁷ often limit laser operation to a lower energy level. At the National Ignition Facility^{8,9} efforts have been made to address this problem by introducing a programmable spot-shadowing system at an upstream image plane. An SLM-based beam-shaping system combined with closed-loop control has been recently demonstrated in a test-bed setup.^{10,11} We have implemented this system in a multiterawatt laser¹² and at the front end of OMEGA EP's long-pulse beamlines.¹³ This effort has revealed a few important issues that need to be addressed for applications in high-power laser systems. Among these, the problem of image distortion will be discussed here, followed by the problem of determining the damage threshold of an SLM device.

Previous work on adaptive beam shaping presented an algorithm based on direct linear mapping between the measured fluence and the command map of an SLM.¹¹ The motivation for direct mapping is to avoid characterizing the enormous number of influence functions associated with an SLM. A linear transformation is experimentally shown to be accurate enough for the imaging systems considered in high-power laser systems. Higher-order distortions such as barrel/pincushion distortions are negligible if the laser beams are image relayed with slow optics. On the other hand, image-distortion effects associated with the presence of tilted plates or wedges in the system are important for this application. As shown in Fig. 127.4, tilted plates/wedges introduce not only astigmatic image blurring¹⁴

but also image shear. Such elements, e.g., beam diagnostic pickoffs, thin-film polarizers, or amplifier slabs, are ubiquitous in high-power lasers. The image shear can be represented as a linear transformation as follows:

$$\begin{pmatrix} x' \\ y' \end{pmatrix} = \begin{pmatrix} 1 & \sigma \\ 0 & 1 \end{pmatrix} \begin{pmatrix} x \\ y \end{pmatrix},$$

where σ is a shear parameter. This linear transformation can be combined with other linear transformations such as translation, magnification, and rotation. As a result, the sheared image can be numerically corrected. The transformation parameters are found by comparing a known phase or amplitude pattern introduced on the SLM and the measured pattern at the diagnostic image by running an optimization routine.

The blurring is caused by the axial astigmatism in the imaging system; i.e., the foci at sagittal and tangential planes are at different locations. Numerical simulations show that the severity of the blurring in the case of parallel plates is proportional to the tilt angle and the thickness of the plate. The wedged plate introduces an additional dependence of the blurring on the wedge angle and the distance from the image plane. Since the blurring limits the resolution of the beam profile to be shaped, it is best to design the optical system to minimize the axial astigmatism. It is possible to significantly reduce the effect by

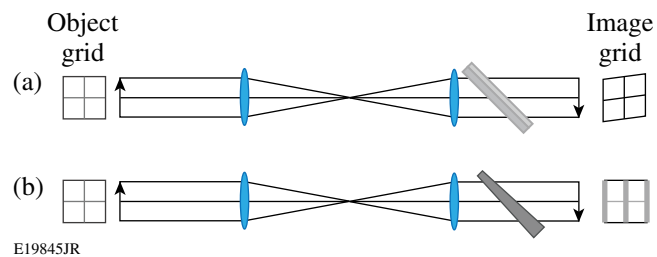


Figure 127.4
Arrangement of wedges and the effects on imaging. A rectangular grid is imaged by a 1-to-1 telescope, where a wedge is placed immediately behind the second lens. The affected image is shown on the right. (a) Image shear occurs when the wedge is placed vertically at an angle. (b) Image blurring occurs in one direction as indicated by the thicker vertical bars in the image grid.

using a compensator plate/wedge,¹⁵ for example, a compensator wedge with the opposite angle.

A schematic of the experimental layout in a multiterawatt system¹² is shown in Fig. 127.5. The laser system is based on optical parametric chirped-pulse amplification (OPCPA) followed by a glass amplifier and compressor chamber. The closed-loop SLM beam-shaping system was implemented using two near-field image feedbacks, one (WFS1 in Fig. 127.5) placed nearby the SLM device and the other (WFS2 in Fig. 127.5) placed at the end of the system before the target chamber. The OPCPA laser beam is image relayed through the glass amplifier to the compressor chamber by three imaging telescopes. There are additional image relays on the diagnostic lines for WFS1 and WFS2 (in the dashed boxes).

The OPCPA front end produces 200-mJ pulses at 5 Hz. Only 10% of full OPCPA energy was used for this experiment and the glass amplifier was turned off. The SLM is an electrically addressed [liquid-crystal-on-silicon (LCOS)], nematic-type liquid crystal made by Hamamatsu. The SLM has 600×792 points, whereas the wavefront sensors have 130×130 sampling points. The wavefront sensors also provide near-field images with the same sampling as wavefront. The case of producing a

flat-top-profile laser beam was first demonstrated with WFS1. The diagnostic imaging system for WFS1 has a wedged leaky mirror that initially caused large spatial registration errors because of the image blurring. A secondary wedge compensator was inserted to restore the image quality. The result of flat-beam shaping is shown in Fig. 127.6. Within the flat area, the peak-to-mode improved from 39% to 12% and the relative rms (root mean square) improved from 9% to 3%.

Closed-loop control with WFS2 proved to be more difficult than with WFS1 because of the axial astigmatism in the system. The astigmatism comes not so much from the amplifier slabs because it is actually minimized by the orthogonal configuration of the slabs on the second pass of the beam. Ray tracing suggests that the astigmatism comes primarily from the compressor gratings. Calculations show that a 20-cm-thick, 1.5° wedge is needed as a compensator, which is not easily available. Therefore, the resolution of the calculated command map on the SLM was intentionally blurred to match the system resolution, which is necessary to prevent the ripple problem of the closed-loop control shaping.¹¹ The fluence distribution improved from 44% to 25% in peak-to-mode as shown in Figs. 127.7(a) and 127.7(b).

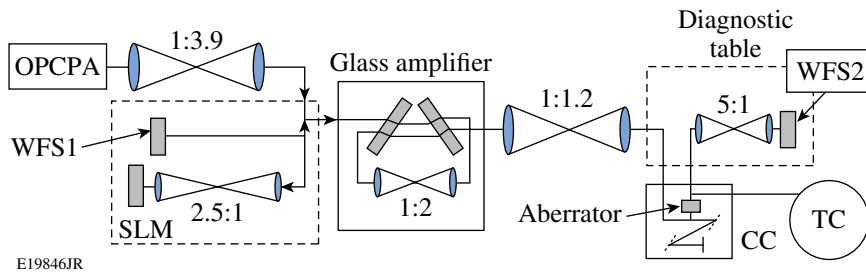


Figure 127.5
Experimental setup for demonstrating an SLM beam shaper in a multiterawatt laser system. CC: compressor chamber; TC: target chamber; WFS: wavefront sensor.

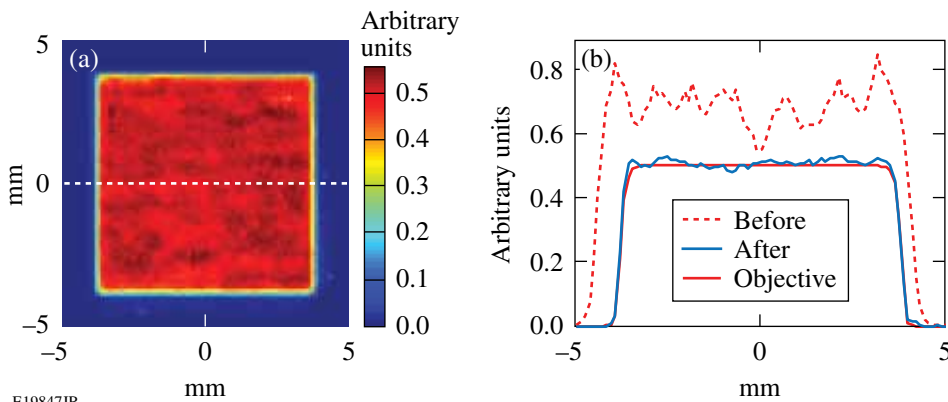
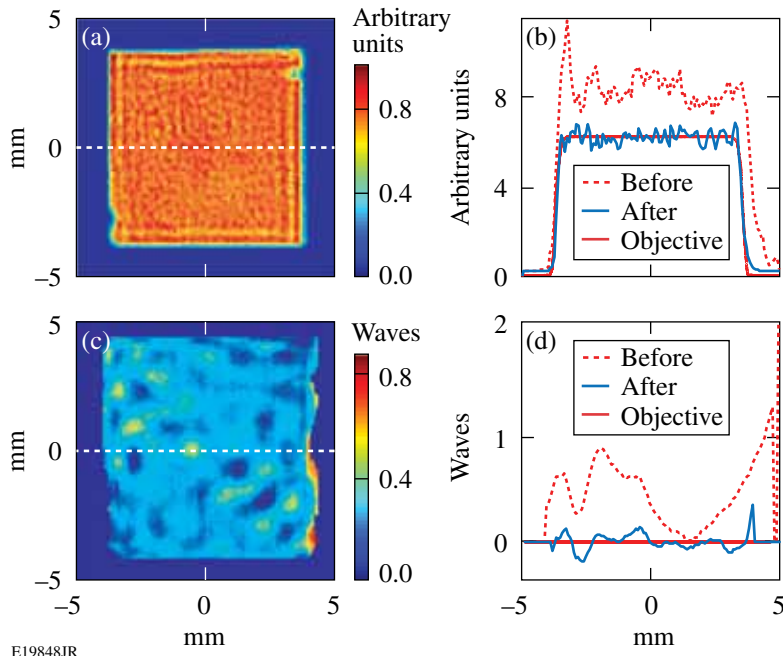


Figure 127.6
Flat-beam shaping with WFS1 (multi-terawatt system). (a) Fluence after shaping; (b) fluence lineouts.

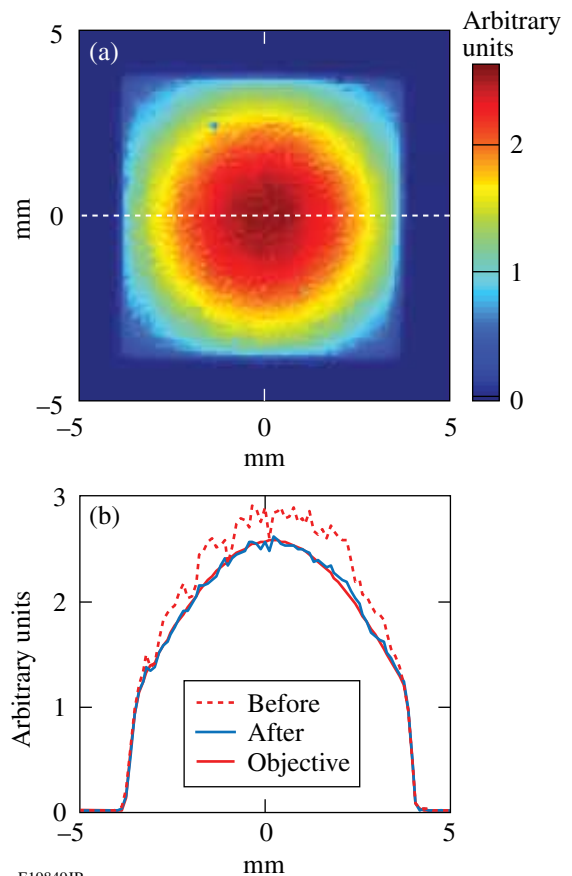


E19848JR

The capability of high-order wavefront correction was tested in WFS2 closed-loop operation. A static wavefront aberrator was manufactured by the magnetorheological finishing process¹² using the map described in Ref. 11. Physical constraints prevented the phase plate from being placed exactly at the image plane of the SLM; therefore, the condition for closed-loop control was not optimum. Nevertheless, the rms value of the wavefront improved from 0.375 waves down to 0.08 waves [Figs. 127.7(c) and 127.7(d)].

The same beam-shaping system has been implemented in the front end of the OMEGA EP long-pulse beamlines. The initial application is to provide intensity smoothing of a beam, which is parabolically shaped by a static apodizer. The parabolic beam shape is used to precompensate for rod-amplifier-gain nonuniformity.¹³ The test confirmed the effectiveness of the direct linear-mapping algorithm for intensity smoothing of a non-flat beam, as shown in Fig. 127.8. A comparable level of convergence error, 2% in relative rms, was achieved as in the OPCPA case. The image shear and rotation were numerically corrected.

Damage-threshold measurements over a small area ($\sim 500 \mu\text{m}$) of an SLM sample with a focused beam resulted in varying values (from 570 mJ/cm^2 to 2 J/cm^2 over ten sites). This suggests that the damage-initiation sites or defects are sparsely distributed over the sample area. The measurement procedure is based on increasing the incident energy by a small step and waiting for a damage spot to occur for minutes of



E19849JR

Figure 127.8
Parabolic beam shaping (OMEGA EP long-pulse front end). (a) Fluence after shaping; (b) fluence lineouts.

duration (a few thousand shots at 5 Hz). The energy is ramped up to the next level until damage is observed where the local fluence for the spot is estimated from the measured laser-beam profile. This procedure often takes several hours for a single site, so it is not practical to perform over hundreds of sites. We performed large-area (~ 5 -mm) damage tests on samples that would effectively enable one to perform hundreds of small-area damage tests in a single ramp-up procedure. The samples were illuminated by 5-Hz, 2.5-ns laser pulses with an $8\text{-mm} \times 8\text{-mm}$ square beam with a flattop profile. The laser pulses were generated from an optical-parametric conversion process at $1.053\text{-}\mu\text{m}$ wavelength. The laser energy on the sample was gradually increased, starting from 50 mJ to 100 mJ in 10-mJ steps. The duration of exposure at each step was 10 min or 3000 shots. The near-field image of the laser beam on the sample was measured every 10 s. The ramping and the short-term exposure continued until a damage site appeared on the near-field image. The local damage fluence at the damage site was calculated based on the separate incident-energy measurement and the calibrated near-field image. The calculated local fluences at the observed damaged sites of the three samples (two of them being under active condition) were 230, 235, and 267 mJ/cm^2 . The minimum of these values can be considered as the damage-threshold fluence. Considering the use area of the SLM to be $\sim 1\text{ cm}^2$ within a $12 \times 16\text{-mm}^2$ total area of the actual device, the total energy the SLM can handle is $\sim 230\text{ mJ}$. The safe energy level can be much lower than this, depending on the local beam modulation of the incident beam.

A successful closed-loop beam shaping was demonstrated in a multiterawatt laser and in an OMEGA EP long-pulse front end. The main issues of implementing an LCOS-SLM beam-shaping system in high-power laser systems have been discussed. It was demonstrated that the imaging-registration problems can be either numerically corrected or avoided by design. The damage threshold of SLM's can be measured by the method described here to ensure safe operations in high-power laser systems. One of the future challenges will be to develop a larger-area or a higher-damage-threshold SLM to accommodate higher-energy operation.

ACKNOWLEDGMENT

This work was supported by the U.S. Department of Energy Office of Inertial Confinement Fusion under Cooperative Agreement No. DE-FC52-08NA28302, the University of Rochester, and the New York State Energy Research and Development Authority. The support of DOE does not constitute an endorsement by DOE of the views expressed in this article.

REFERENCES

1. C. Dorrer, *Opt. Lett.* **34**, 2330 (2009).
2. B. Wattellier *et al.*, *J. Opt. Soc. Am. B* **20**, 1632 (2003).
3. O. Boyko *et al.*, *Opt. Commun.* **246**, 131 (2005).
4. N. Sanner *et al.*, in *Conference on Lasers and Electro-Optics* (Optical Society of America, Washington, DC, 2004), Vol. 1, Paper CTuP34.
5. J. Bourderionnet *et al.*, *Opt. Lett.* **26**, 1958 (2001).
6. J. Qiao, A. W. Schmid, L. J. Waxer, T. Nguyen, J. Bunkenburg, C. Kingsley, A. Kozlov, and D. Weiner, presented at the 2010 International Committee on Ultra-High Intensity Lasers Conference, Watkins Glen, NY, 26 September–1 October 2010 (Paper FO3).
7. A. Conder *et al.*, in *Laser-Induced Damage in Optical Materials: 2007*, edited by G. J. Exarhos *et al.* (SPIE, Bellingham, WA, 2007), Vol. 6720, p. 672010.
8. S.-W. Bahk, J. D. Zuegel, J. R. Fienup, C. C. Widmayer, and J. Heebner, *Appl. Opt.* **47**, 6586 (2008).
9. J. Heebner *et al.*, in *Laser-Induced Damage in Optical Materials: 2010*, edited by G. J. Exarhos *et al.* (SPIE, Bellingham, WA, 2010), Vol. 7842, p. 78421C.
10. V. Bagnoud and J. D. Zuegel, *Opt. Lett.* **29**, 295 (2004).
11. S.-W. Bahk, E. Fess, B. E. Kruschwitz, and J. D. Zuegel, *Opt. Express* **18**, 9151 (2010).
12. V. Bagnoud, M. J. Guardalben, J. Puth, J. D. Zuegel, T. Mooney, and P. Dumas, *Appl. Opt.* **44**, 282 (2005).
13. M. J. Guardalben and L. J. Waxer, in *High Power Lasers for Fusion Research*, edited by A. A. S. Awwal, A. M. Dunne, H. Azechi, and B. E. Kruschwitz (SPIE, Bellingham, WA, 2011), Vol. 7916, Paper 79160G.
14. R. Korniski and J. K. Lawson, in *International Optical Design Conference, 2002 OSA Technical Digest Series* (Optical Society of America, Washington, DC, 2002), Paper ITuD5.
15. J. W. Howard, *Appl. Opt.* **24**, 4265 (1985).

Temporal Contrast Degradation at the Focus of Ultrafast Pulses from High-Frequency Spectral Phase Modulation

Introduction

Ultrafast laser systems generate intensities at focus as high as 10^{22} W/cm² for a variety of relativistic and high-energy-density physics applications. Although several types of amplifiers are used, all systems use chirped-pulse amplification (CPA) to overcome limits caused by optical damage and nonlinearities.¹ CPA uses stretchers and compressors to modify the pulse's spectral phase, increasing its length and lowering the peak power within the amplifier chain. Stretchers and compressors typically rely on diffraction gratings to geometrically disperse the pulse into spectral components.² Imperfections at optical surfaces where the pulse is dispersed imprint directly onto the spectral phase. The group delay of a spectral component equals the derivative of its phase, and therefore high-frequency phase noise scatters energy before and after the main pulse.^{3–6} (This effect is directly analogous to the halo formed around the far field of a lens by high-frequency wavefront noise in the near field.⁷) Any portion scattered before the peak of the pulse that exceeds 10^{11} W/cm² is capable of ionizing solid targets. Therefore, care is needed when selecting stretchers and compressors to ensure they do not degrade the temporal contrast of the laser system, defined as the ratio of the peak of the pulse to the low-intensity pedestal.

This article presents a theoretical analysis of the impact of high-frequency spectral phase modulation on the temporal contrast of ultrafast pulses. A three-dimensional (3-D) treatment is used to extend the results of Ref. 8. The temporal contrast is evaluated in the focal plane, the target location for ultra-intense experiments. The spectral phase imprint in the near field of a spectrally dispersed beam produces space–time coupling in the far field or focal plane. The pedestal is swept across an area in the focal plane many times the size of the diffraction-limited spot. These phenomena raise questions about the validity of applying measurements made in the near field (the usual domain for high-dynamic-range cross-correlators) to the target plane.

A general model is used in the next section to propagate a spectrally dispersed beam through a noisy phase screen.

Expressions are derived for the average intensity of an ultrafast pulse in the near and far fields. In subsequent sections, closed-form results are obtained for Gaussian functional forms that show the impact on temporal contrast of the scale of optical surface modulation, the beam size, and the scale of geometric dispersion in the near field. Analytic results are compared to numeric simulations, and the numeric analysis is extended to include the usual Lorentzian functional form of the power spectral density of optical surfaces. Simulation results are presented for generic stretchers and compressors that show fundamentally different properties of the temporal contrast at the focal plane.

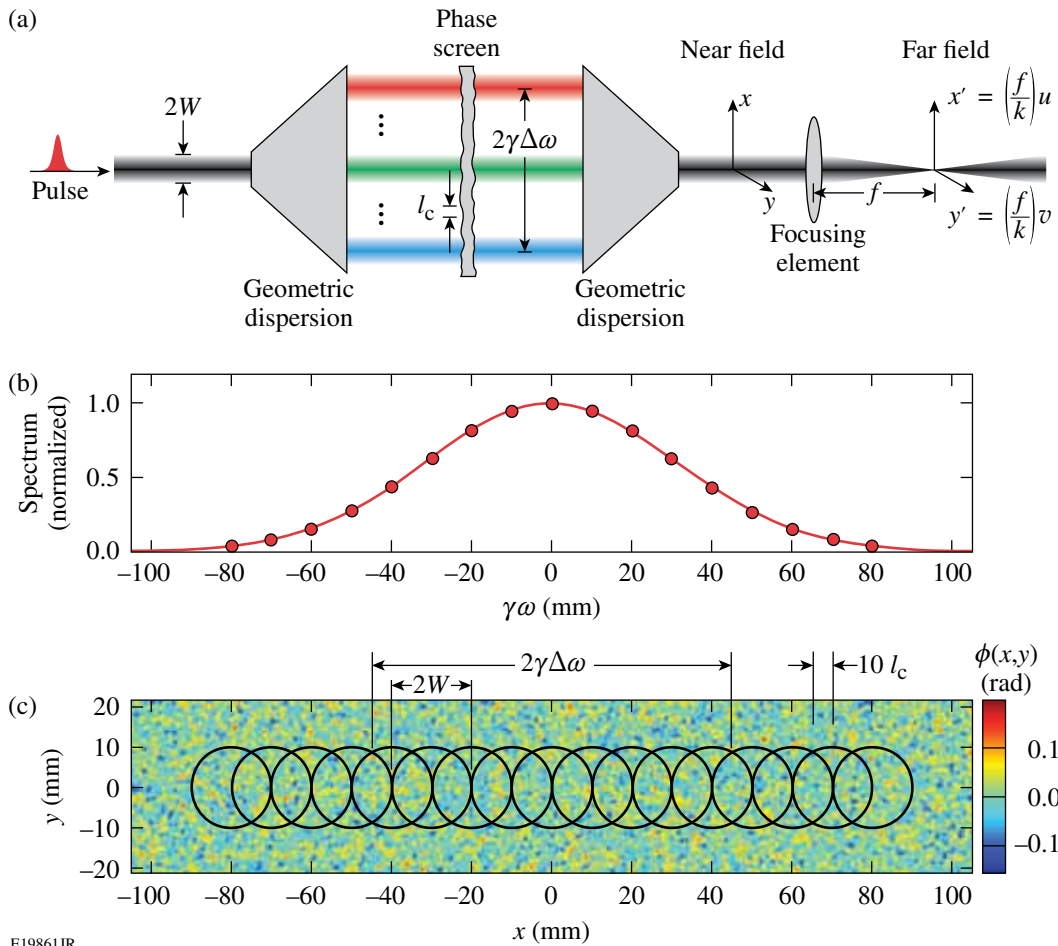
General Expressions for the Temporal Contrast in Near and Far Fields

1. Model

A general schematic of an optical device for spectral phase modification is shown in Fig. 127.9(a). A beam of optical pulses passes through a subsystem that spreads the spectral components using geometric dispersion. The phase of each spectral component is modified using phase screens or other optical systems before a second dispersive component is used to recombine them. Optical pulse stretchers and compressors are examples of this type of device. They modify the chirp of ultrafast pulses by adding or subtracting large, predominantly quadratic spectral phases. High-frequency imperfections in the surface quality of their optics produce unwanted phase modulation. In this article, such imperfections are modeled by adding noisy phase screens to otherwise ideal systems.

A focusing element located in the near field focuses the beam in the far-field plane. The near-field spatial coordinates are (x,y) . The far-field wave-vector components (u,v) are related to the spatial coordinates (x',y') by the focal length f and wave number $k = 2\pi/\lambda$ according to $u = kx'/f$. Figure 127.9(b) shows a Gaussian spectrum spread across the near field. The mapping of spectral components onto the x axis is assumed to be linear. The center of the beam x_0 and a given optical frequency ω are related by

$$x_0(\omega) = \gamma\omega, \quad (1)$$



EI9861JR

Figure 127.9

(a) Generic schematic of a system that imprints spectral phase noise on an optical pulse propagating with a finite beam size. The near-field spatial coordinates are (x, y) and the far-field wave-vector components are (u, v) . Three important scale lengths are (1) $\gamma\Delta\omega$, the spatial width of the dispersed spectrum; (2) W , the beam size; and (3) l_c , the correlation length of the phase noise. (b) Gaussian spectrum plotted against the near-field coordinate x ; $\gamma = 0.44$ mm/THz and $\Delta\omega = 100$ THz, corresponding to a 17-fs pulse width. (c) Simulated phase screen $\phi(x, y)$ and beam locations for optical frequencies marked in (b). Scale lengths are $W = 10$ mm, $l_c = 0.5$ mm, and $\gamma\Delta\omega = 44$ mm.

where γ is the spatio-spectral coefficient. The optical frequency ω is defined as the offset from a central frequency ω_0 , which was arbitrarily chosen to correspond to a central wavelength of 910 nm throughout this article.

Figure 127.9(c) shows a simulated realization of a random phase screen, $\phi(x, y)$. The circles denote the beam locations for the spectral components marked on Fig. 127.9(b). Three scale lengths are shown that are key to understanding the impact of phase noise on temporal contrast:

- $\gamma\Delta\omega$ – the optical bandwidth ($1/e$ half-width), scaled onto the near-field axis
- W – the beam size ($1/e$ intensity half-width)
- l_c – the correlation length of the phase noise

Here, l_c can be defined in terms of the correlation function

$$C(x, x', y, y') = \langle \phi(x, y) \phi^*(x', y') \rangle. \quad (2)$$

For a homogeneous, isotropic Gaussian phase screen, the correlation function is related to the correlation length by

$$C(\Delta x, \Delta y) = \sigma^2 \exp\left(-\frac{\Delta x^2 + \Delta y^2}{2l_c^2}\right), \quad (3)$$

where $\Delta x = x - x'$, $\Delta y = y - y'$, and σ is the rms (root mean square) phase of the screen in radians. Depending on the design of the device, the three scale lengths may differ by an order of magnitude or more.

2. Average Far-Field Intensity

In the spectral domain, the optical field of the pulse in the near field is given by

$$\tilde{E}(x, y, \omega) = \tilde{E}_0(x, y, \omega) e^{i\Phi(x, y, \omega)}, \quad (4)$$

where $\tilde{E}_0(x, y, \omega)$ is the input pulse. The spatio-spectral phase function $\Phi(x, y, \omega)$ is related to the phase screen using Eq. (1):

$$\Phi(x, y, \omega) = \phi(x - x_0, y) = \phi(x - \gamma\omega, y). \quad (5)$$

In the limit of small phase modulation ($\phi \ll 1$), the exponential in Eq. (4) is approximated to give

$$\tilde{E}(x, y, \omega) = \tilde{E}_0(x, y, \omega) [1 + i\phi(x - \gamma\omega, y)]. \quad (6)$$

The optical field in the time domain is obtained by a Fourier transform:

$$\begin{aligned} E(x, y, t) &= \int_{-\infty}^{\infty} d\omega \tilde{E}(x, y, \omega) e^{-i\omega t} \\ &= E_0(x, y, t) \\ &\quad + i \int_{-\infty}^{\infty} d\omega \tilde{E}_0(x, y, \omega) \phi(x - \gamma\omega, y) e^{-i\omega t}. \end{aligned} \quad (7)$$

In the far field of a focusing element, the optical field can be expressed in terms of wave-vector components (u, v) , as denoted in Fig. 127.9(a). The double Fourier transform of Eq. (7) gives

$$\begin{aligned} \check{E}(u, v, t) &= \int_{-\infty}^{\infty} \int_{-\infty}^{\infty} dx dy E(x, y, t) e^{-iux} e^{-ivy}, \\ &= \check{E}_0(u, v, t) + i \int_{-\infty}^{\infty} \int_{-\infty}^{\infty} \int_{-\infty}^{\infty} d\omega dx dy \\ &\quad \times \tilde{E}_0(x, y, \omega) \phi(x - \gamma\omega, y) e^{-i(\omega t + ux + vy)}. \end{aligned} \quad (8)$$

The intensity in the far field is $I(u, v, t) = |\check{E}(u, v, t)|^2$. Averaging over an ensemble of phase screens for which $\langle \phi(x, y) \rangle = 0$, the average intensity in the far field is

$$\begin{aligned} \langle I(u, v, t) \rangle &= I_0(u, v, t) + \int_{-\infty}^{\infty} \dots \int_{-\infty}^{\infty} d\omega d\omega' dx dx' dy dy' \\ &\quad \times \tilde{E}_0(x, y, \omega) \tilde{E}_0^*(x', y', \omega') \\ &\quad \times \langle \phi(x - \gamma\omega, y) \phi^*(x' - \gamma\omega', y') \rangle \\ &\quad \times e^{-i(\omega - \omega')t} e^{-i(x - x')u} e^{-i(y - y')v}. \end{aligned} \quad (9)$$

Using a coordinate transformation and completing four integrals [see **Appendix A** (p. 128)], the average far-field intensity can be written in terms of the power spectral density (PSD) of the phase screen:

$$\begin{aligned} \langle I(u, v, t) \rangle &= I_0(u, v, t) \\ &\quad + \int_{-\infty}^{\infty} \int_{-\infty}^{\infty} du' dv' I_0(u', v', t' + \gamma u - \gamma u') \\ &\quad \times \text{PSD}(u - u', v - v'). \end{aligned} \quad (10)$$

Equation (10) is an integral expression for the average far-field intensity given the PSD of the phase screens and I_0 , the far-field intensity without a phase screen. Further analysis is only possible if one assumes functional forms for the integrand.

3. Average Near-Field Intensity

An expression for the average intensity in the near field can be derived using a similar formalism. One starts with an expression similar to Eq. (9), but with all quantities defined in the near field, thereby eliminating the four integrals over the near-field coordinates:

$$\begin{aligned} \langle I(x, y, t) \rangle &= I_0(x, y, t) \\ &\quad + \int_{-\infty}^{\infty} \int_{-\infty}^{\infty} d\omega d\omega' \tilde{E}_0(x, y, \omega) \tilde{E}_0^*(x, y, \omega') \\ &\quad \times \langle \phi(x - \gamma\omega, y) \phi^*(x - \gamma\omega', y) \rangle e^{-i(\omega - \omega')t}. \end{aligned} \quad (11)$$

In this case, it is convenient to use a one-dimensional (1-D) correlation function where the near-field coordinates (x, y) are parameters:

$$C_{xy}(\Delta\omega) = \langle \phi(x - \gamma\omega, y) \phi^*(x - \gamma\omega', y) \rangle. \quad (12)$$

Performing the same coordinate transformation as outlined in **Appendix A** (p. 128), replacing the 1-D correlation function with its Fourier transform PSD_{xy} , and completing integrals of exponentials and a delta function give the following:

$$\langle I(x, y, t) \rangle = I_0(x, y, t) + \int_{-\infty}^{\infty} dt' I_0(x, y, t') \text{PSD}_{xy}(t - t'). \quad (13)$$

That is, the average near-field intensity has an additional term as a result of phase noise that is the convolution of the noise-free intensity and the 1-D power spectral density. This near-field result is similar to that derived in Ref. 8, but without the stated approximations.

The connection between the two-dimensional (2-D) and 1-D PSD functions, $\text{PSD}(u, v)$ and $\text{PSD}_{xy}(t)$, is derived in **Appendix B** (p. 129) and is

$$\text{PSD}_{xy}(t) = \frac{1}{\gamma} \int_{-\infty}^{\infty} dv \text{PSD}(t/\gamma, v). \quad (14)$$

That is, the 1-D temporal PSD is proportional to the integral of the 2-D spatial PSD over one spatial frequency axis after the other axis—the one that defines the plane of geometric dispersion—is replaced by the scaled time axis using $u = t/\gamma$.

Analytic Expressions Assuming Gaussian Functional Forms

It is instructive to consider the case where all quantities are Gaussians. That is, the 2-D PSD function of the phase screen has a Gaussian functional form, as well as the beam profile and the pulse shape. In this case, the integral expressions for the average intensity in the far field [Eq. (10)] and near field [Eq. (13)] can be reduced to closed-form analytic expressions. The PSD is the Fourier transform of Eq. (3):

$$\text{PSD}(u, v) = \frac{\sigma^2 l_c^2}{2\pi} \exp\left[-l_c^2(u^2 + v^2)/2\right]. \quad (15)$$

The noise-free intensity is

$$I_0(u, v, t) = I_P \exp(-\Delta\omega^2 t^2 - W^2 u^2 - W^2 v^2), \quad (16)$$

where I_P is the peak, on-axis intensity at $u = v = t = 0$. The pulse width τ_0 (defined as the half-width at the $1/e$ intensity) is equal to $1/\Delta\omega$. Similarly, the width of the focal spot, w_0 (defined as

the half-width at $1/e$ intensity), is equal to $1/W$. Substitution into Eq. (10) gives

$$\begin{aligned} \langle I(u, v, t) \rangle &= I_0(u, v, t) \\ &+ I_P \frac{\sigma^2 l_c^2}{2W} \left(l_c^2/2 + \gamma^2 \Delta\omega^2 + W^2 \right)^{-1/2} \\ &\times \exp\left[\frac{(\gamma\Delta\omega^2 t - W^2 u)^2}{l_c^2/2 + \gamma^2 \Delta\omega^2 + W^2} \right] \\ &\times \exp\left(-W^2 u^2 - l_c^2 v^2/2 - \Delta\omega^2 t^2 \right). \end{aligned} \quad (17)$$

The second term is the low-intensity pedestal that is produced by the phase screen. The magnitude of the pedestal scales with the variance of the phase, σ^2 . One limit that is often the case for stretchers and small-scale compressors is that the spatial spread of the spectrum across the phase screen ($\gamma\Delta\omega$) is much larger than both the input beam size (W) and the correlation length (l_c). Typical values for the three quantities are of the order of 100 mm, 1 mm, and 100 μm , respectively. Using this limit, the far-field intensity can be approximated as

$$\begin{aligned} \langle I(u, v, t) \rangle &= I_0(u, v, t) + I_P \frac{\sigma^2 l_c}{\sqrt{2} \gamma \Delta\omega} \left(\frac{l_c}{\sqrt{2} W} \right) \\ &\times \exp\left[-W^2 \left(u + \frac{t}{\gamma} \right)^2 - \frac{l_c^2 v^2}{2} - \frac{l_c^2 t^2}{2\gamma^2} \right]. \end{aligned} \quad (18)$$

The expression for the near-field intensity has a similar form, where I_P is the peak intensity in the near field:

$$\langle I(x, y, t) \rangle = I_0(x, y, t) + I_P(x, y) \frac{\sigma^2 l_c}{\sqrt{2} \gamma \Delta\omega} \exp\left(-\frac{l_c^2 t^2}{2\gamma^2} \right). \quad (19)$$

There are several important differences between these two expressions. First, the noise-dependent terms at the peak of the pulse differ by the factor $l_c/\sqrt{2}W$. Typically this factor is much less than unity. Therefore one could expect a much smaller on-axis, noise-dependent contribution in the vicinity of $t = 0$ in the far field than in the near field.

The second and more significant difference is the presence of the space–time coupling term in the exponent: $-W^2(u + t/\gamma)^2$. As a result, the maximum far-field intensity of the pedestal at a given time corresponds to a different transverse location in the far field. The location is determined from the equation

$u = -t/\gamma$. More general results, discussed below, support this conclusion. This space–time coupling is analogous to that reported in certain types of pulse shapers.⁹ In summary, these analytic results, although derived specifically for Gaussian functional forms, show that one should expect large differences between the temporal contrast in the near and far fields.

Comparison of Analytic Results and Numerical Simulations

The analytic expressions were tested against numerical simulations of spatially dispersed ultrafast pulses propagating through phase screens. Table 127.I shows default model parameters, unless explicitly specified. The 2-D PSD function was used to generate a random phase screen of Gaussian random numbers over the entire near-field plane in the dispersed region.¹⁰ An input beam was dispersed into spectral components that were incident on different sections of the phase screen, as shown in Fig. 127.9(c). Beams of each component

were modulated by the screen and then propagated to the far field using 2-D fast Fourier transforms (FFT's). Each spectral component was added coherently. The far-field intensity at each position (u,v,t) was calculated as the magnitude of the total field squared. To avoid noise from interpolation, the near-field and spectral sampling intervals were matched using the spatio-spectral coefficient so that $\delta x = \gamma \delta \omega$.

Figures 127.10–127.12 compare numerical simulations to the analytic results for Gaussian functional forms. The near-field average intensity in the x – t plane is shown in Fig. 127.10(a). The intensity is plotted on a logarithmic scale in dB relative to the peak. The narrow peak down the center around $t = 0$ is the intense, noise-free term $I_0(x,y,t)$ in Eq. (19). The low-intensity pedestal comes from the second, PSD-driven term. In Figs. 127.10(b)–127.10(d) numerical simulations for a single-phase screen realization and the analytic average are compared at three different x positions in the near field. While

Table 127.I: Default simulation parameters used in this article, unless explicitly specified.

Parameter	Symbol	Value	Parameter	Symbol	Value
Center wavelength	λ_0	910 nm	Time step	δt	8 fs
1/e pulse half-width	τ_0	10 fs	Number of time steps	N_T	2^{12}
Near-field beam size	W	1 mm	Near-field step	δx	84 μm
Spatiospectral coefficient	γ	0.44 mm/THz	Number of steps across beam	N_X	2^8
rms phase	σ	0.04 rad	Frequency step	$\delta \omega$	0.19 THz
Correlation length	l_c	100 μm	Phase screen dimensions	$x_{\text{max}}, y_{\text{max}}$	360 \times 21 mm

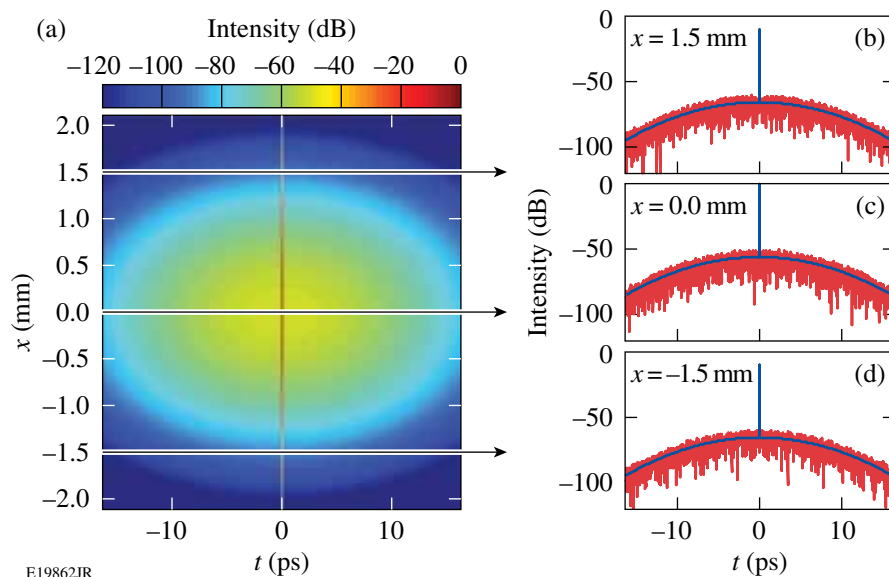


Figure 127.10

(a) Near-field average intensity in the x – t plane calculated using Eq. (19). The main pulse $I_0(x,y,t)$ is the red line at $t = 0$ ps. [(b),(c),(d)] Analytic (blue) and numeric (red) values of intensity calculated at different x values.

E19862JR

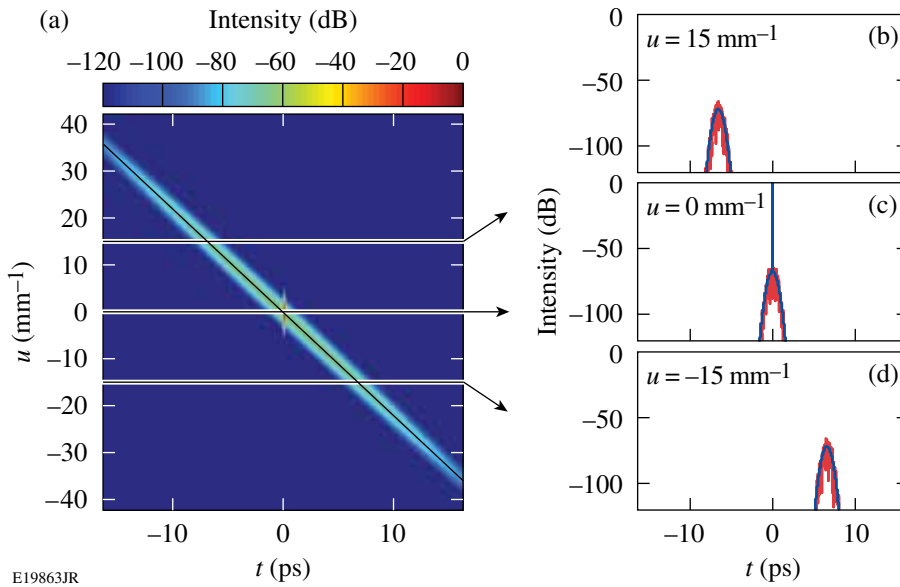


Figure 127.11

(a) Far-field average intensity in the u - t plane calculated using Eq. (18). Space-time coupling in the noise-dependent term follows the black line, $u = -t/\gamma$. [(b),(c),(d)] Analytic (blue) and numeric (red) values of intensity calculated at different u values.

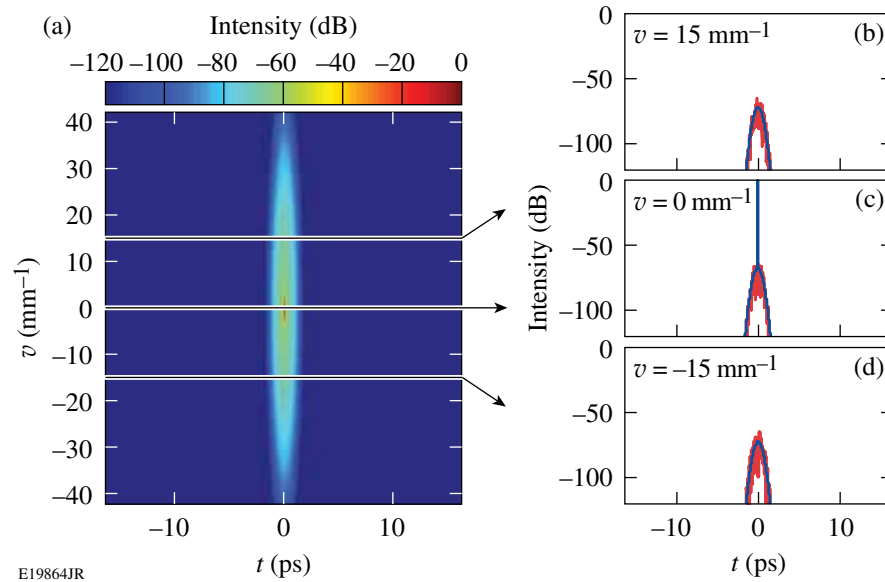


Figure 127.12

(a) Far-field average intensity in the v - t plane calculated using Eq. (17). [(b),(c),(d)] Analytic (blue) and numeric (red) values of intensity calculated at different v values.

the numerical results (red lines) have high-frequency structure, which is a consequence of using a single-phase screen realization, their overall profile follows the analytic results (blue lines).

Results calculated for the far field in the u - t plane, using Eq. (18), are shown in Fig. 127.11. The space-time coupling between u and t appears as a diagonal noise-dependent contribution to the intensity that follows $u = -t/\gamma$. As a consequence, the slices at different u positions show a temporal displacement of the noise-dependent term. In contrast, plots in the v - t plane (Fig. 127.12) do not show space-time coupling. The v axis is conjugate to the y axis, which is orthogonal to the plane of spectral dispersion.

The temporal narrowing on axis in the far field ($u = v = 0$) depends on W , the size of the beam in the near field. Figure 127.13 shows results for four values of W . The far-field intensity approaches the near-field result as the size of the beam is reduced from 3 to 0.1 mm. In this small-beam limit, each spectral component samples only a small portion of the screen, and the statistics become identical to the 1-D case for the near field. The beneficial effect of averaging the phase contributions over multiple correlation lengths no longer occurs, and the on-axis contrast is reduced.

The numeric results have high-frequency structure because they used a single realization of the phase screen. Averag-

ing over multiple pulses (each calculated using a different phase screen) increases the level of agreement between the numeric and analytic results in both the near and far fields (see Fig. 127.14).

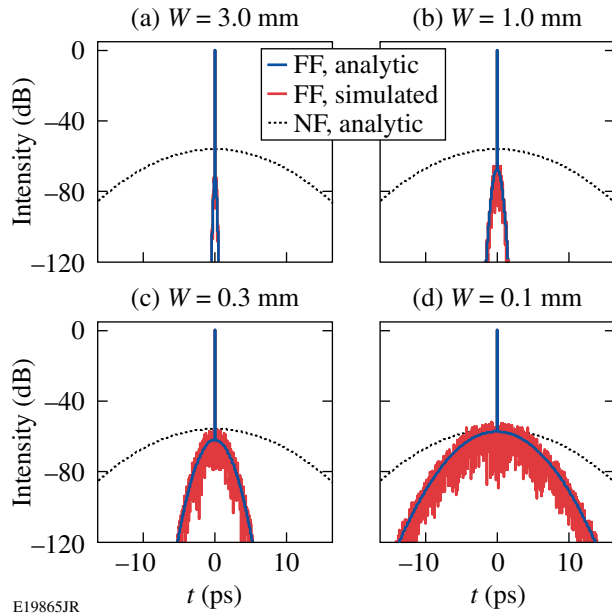


Figure 127.13

On-axis temporal intensities for Gaussian functional forms and a range of near-field beam sizes (W). The on-axis far-field contrast increases with the beam size.

In principle, there can be significant differences between temporal and ensemble averages for non-ergodic phenomena. Since a laser's stretcher or compressor typically uses static optics, an ensemble average over many phase screens is not relevant. Intensity averaging in time may occur, however, depending on the nature of the interaction with a target. The physical processes may not respond quickly enough to follow the high-frequency temporal modulation. In this case, the relevant quantity is the temporal average of the intensity over the response time of the interaction.

Figure 127.15 shows on-axis plots of the intensity in the near field and far field. The red line is a box-car average in time of the temporal intensity from a single realization of the phase screen. The black line is an ensemble average over pulses that were each calculated using an independent realization of the phase screen. The overall profiles are similar; therefore, one can treat intensity noise from phase screens in spectrally dispersed beams as an ergodic process.

The statistical nature of the intensity fluctuations at a given time may be relevant if the target interaction is nonlinear. In

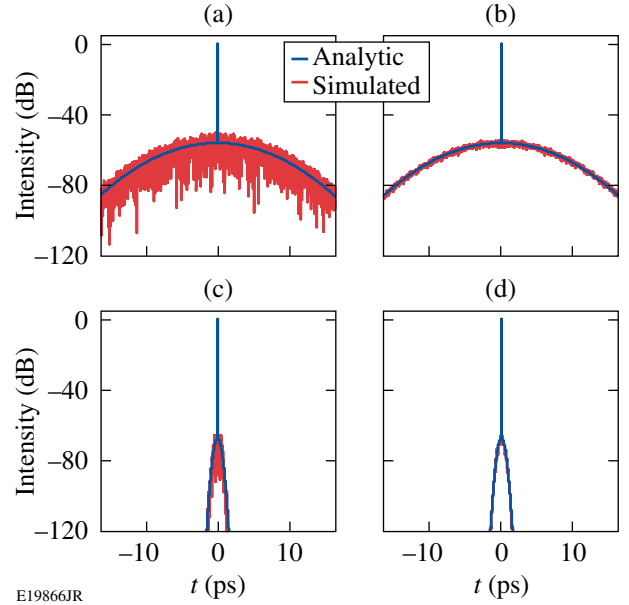


Figure 127.14

On-axis temporal intensities for Gaussian functional forms. Near-field results for (a) one phase screen and (b) an ensemble average of pulses for 25 phase screens. Far-field results for (c) one phase screen and (d) an ensemble average of pulses for 25 phase screens.

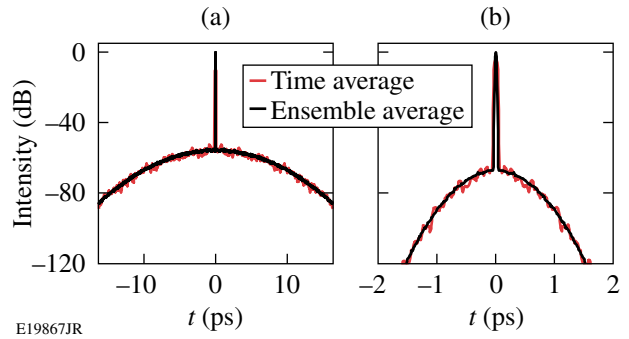


Figure 127.15

Average on-axis intensity calculated either by averaging in time (rectangular window, T) or over an ensemble of phase maps (N). (a) Near-field intensity: $T = 200$ fs, $N = 200$; (b) far-field intensity: $T = 40$ fs, $N = 200$.

general, the intensity-probability distribution for the coherent addition of two beams, one uniform and one statistically fluctuating with a uniform phase distribution $[0, 2\pi]$, is given by¹¹

$$p(I) = \frac{1}{\langle I \rangle} \exp\left(-r - \frac{I}{\langle I \rangle}\right) \mathbf{I}_0\left(2\sqrt{rI/\langle I \rangle}\right), \quad (20)$$

where \mathbf{I}_0 is the modified Bessel function of the first kind of order zero and $r = I_0/\langle I \rangle$. At times where the intensity of the noise-free pulse, I_0 , is much less than that of the pedestal, the parameter $r \ll 1$ and Eq. (19) may be approximated by

$$p(I) \approx \frac{1}{\langle I \rangle} \exp\left(-\frac{I}{\langle I \rangle}\right). \quad (21)$$

Figure 127.16 shows the probability density of the intensity in both the near and far fields at $t = 250$ fs, calculated using an ensemble of phase maps. The numeric results for 200 phase screens are in agreement with the probability calculated using Eq. (21), shown in red.

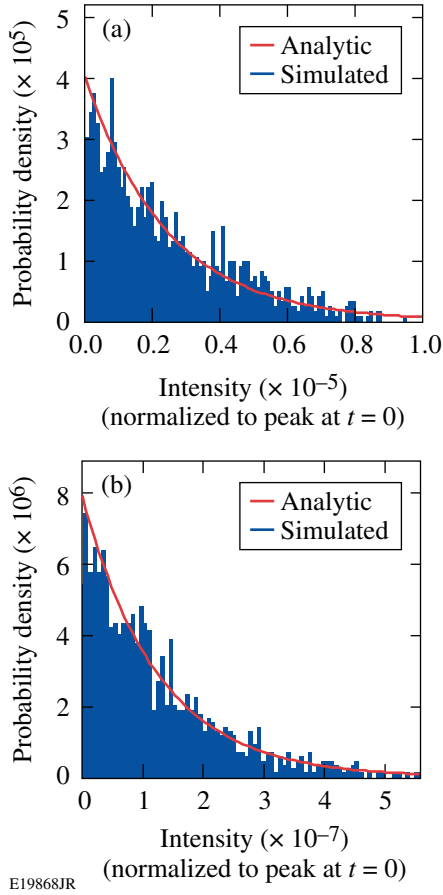


Figure 127.16
Intensity probability distributions at $t = 250$ fs for (a) the near field and (b) the far field.

Lorentzian PSD Functional Forms

Gaussian PSD's are convenient for obtaining closed-form analytic expressions that show the relative impact of the three main scale lengths: $\gamma\Delta\omega$, W , and l_c . In practice, however, optical surfaces do not have Gaussian PSD's. More common are PSD's with a Lorentzian functional form.¹²

$$\text{PSD}(u,v) = \frac{(S-1)\sigma^2 l_c^2}{2\pi(1+l_c^2 u^2 + l_c^2 v^2)^{(S+1)/2}}. \quad (22)$$

The parameter S is the asymptotic slope of the 1-D PSD function. Following Eq. (14), the 1-D PSD in the time domain is

$$\text{PSD}_{xy}(t) = \frac{\sigma^2 l_c \Gamma(S/2)}{\sqrt{\pi} \gamma \Gamma\left(\frac{S-1}{2}\right) \left(1 + l_c^2 t^2 / \gamma^2\right)^{S/2}}, \quad (23)$$

which scales as $1/t^S$ for large times ($t \gg \gamma/l_c$). Typical values of S are in the range of 1.5 to 1.6 (Ref. 12). Despite differences in the functional forms of the Lorentzian and Gaussian PSD's, Fig. 127.17 shows that the nature of the near- and far-field temporal intensities for Lorentzians is qualitatively similar except for a slower fall-off far from the peak.

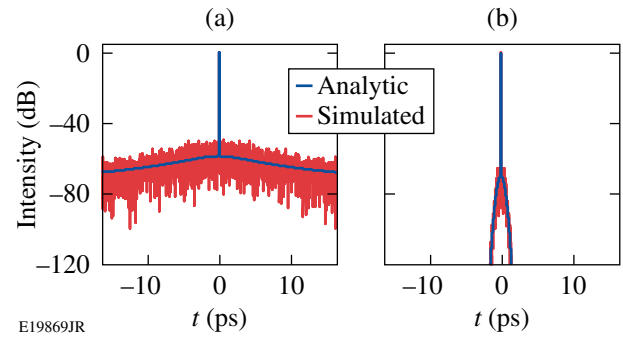


Figure 127.17
On-axis temporal intensity calculated in (a) near field and (b) far field for a Lorentzian PSD with $\sigma = 0.04$ radians, $l_c = 100 \mu\text{m}$, and $S = 1.55$.

Application of Results to Stretchers and Compressors

1. Systems with Multiple Elements

Pulse stretchers and compressors are commonly used in ultrafast CPA laser systems to raise the limits for damage and nonlinearity in their optical amplifiers. Pulses must pass through an even number of dispersing elements such as gratings or prisms to eliminate residual angular dispersion. Additional optical components may be required in portions of the system where the pulse is geometrically dispersed; therefore their surface quality will affect the pulse's temporal contrast. One example is the case of an Öffner stretcher.¹³ Here, two spherical mirrors are used to create an image of a diffraction grating at a "negative" distance from the object, resulting in net positive dispersion for the pulse. It has been shown that the surface quality of stretcher mirrors⁴ and gratings⁶ can have a significant impact on the temporal contrast of the pulse.

It is important, therefore, to be able to apply the preceding results, derived for a single phase screen, to systems with several phase screens. If the phase screens are practically

coincident or imaged onto each other, their phases are summed using the appropriate spatio-spectral coefficients, to get a total phase screen:

$$\Phi_{\text{total}}(x, y, \omega) = \sum_n \phi_n(x - \gamma_n \omega, y). \quad (24)$$

If the phase screens are uncorrelated, the correlation function for the total phase reduces to a sum of correlation functions:

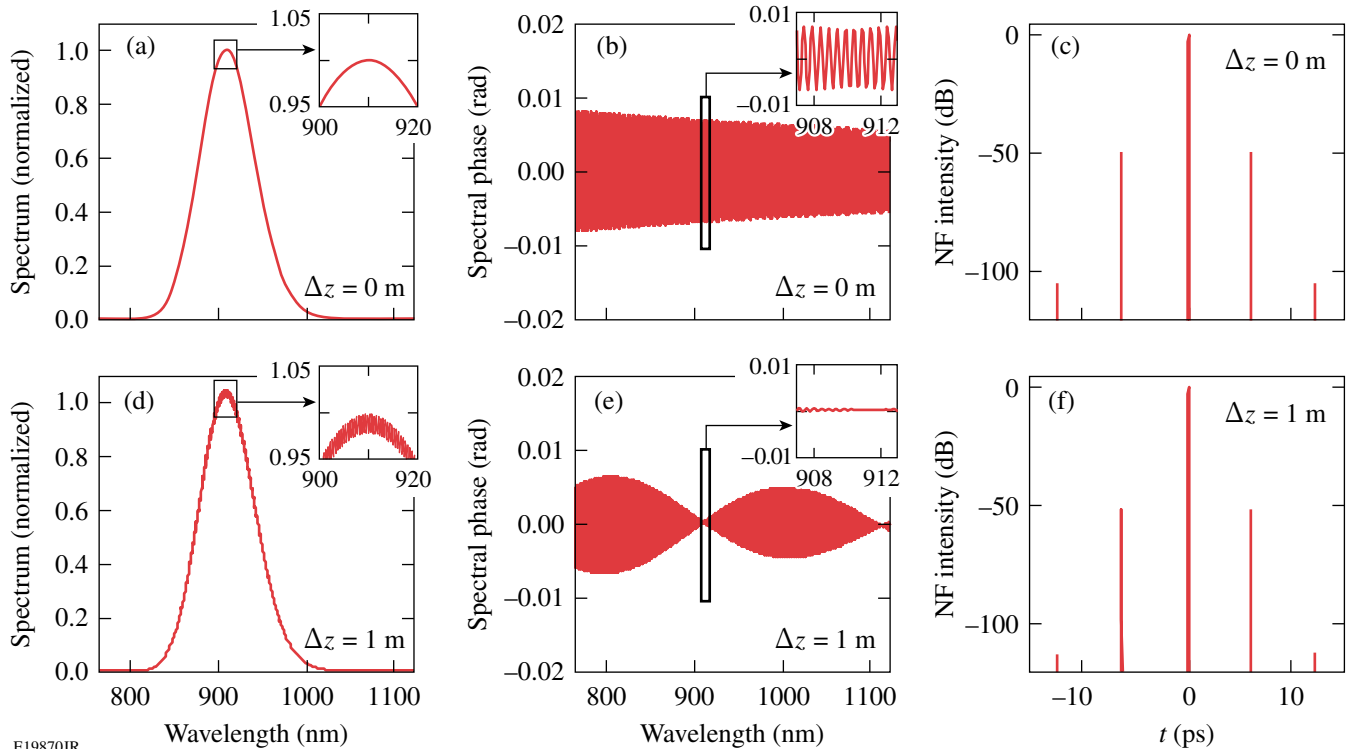
$$\langle \Phi_{\text{total}}(x, y, \omega) \Phi_{\text{total}}^*(x', y', \omega') \rangle = \sum_n C_n(\Delta x - \gamma_n \Delta \omega, \Delta y). \quad (25)$$

In the expressions for the average intensity in the near field or far field, the noise-dependent term becomes a sum over the PSD of each phase screen. For example, in the far field, the average intensity is

$$\begin{aligned} \langle I(u, v, t) \rangle &= I_0(u, v, t) \\ &+ \sum_n \int_{-\infty}^{\infty} \int_{-\infty}^{\infty} du' dv' I_0(u', v', t' + \gamma_n u - \gamma_n u') \\ &\times \text{PSD}_n(u - u', v - v'). \end{aligned} \quad (26)$$

Typically, however, the phase screens are not coincident or imaged onto each other. Significant distances of free propagation (of the order of a meter) are often required to obtain the desired amount of dispersion. In this case, propagation between the surfaces causes high-frequency phase modulation to be converted into amplitude modulation, and vice versa. The distance required for complete phase-to-amplitude conversion is derived from the Talbot effect and is equal to $\Delta x^2/2\lambda$, where Δx is the modulation period.^{14,15} The high-frequency modulation relevant to ultrafast pulse contrast may have periods as short as $100 \mu\text{m}$, for which the phase-to-amplitude conversion distance at $1 \mu\text{m}$ is only 5 mm.

A full description, analytical or numerical, that includes diffraction is complicated. Such an approach, however, is not required when estimating the overall impact on temporal contrast from a series of phase screens. Although near-field propagation changes the fine-scale structure, it has only a minor effect on the average intensity. This is because amplitude modulation degrades the temporal contrast in a way that is very similar to phase modulation. This is shown in Fig. 127.18, where



E19870JR

Figure 127.18

Near-field quantities after spectrally dispersed propagation through a sinusoidal phase screen with a modulation period and amplitude of $450 \mu\text{m}$ and 0.5 nm , respectively. (a) The spectrum, (b) spectral phase, and (c) temporal intensity immediately after the screen. [(d),(e),(f)] The same quantities after propagating a distance of 1 m. There is complete conversion of phase-to-amplitude modulation at the peak wavelength of 910 nm .

the near-field properties of a pulse (spectrum, spectral phase, and temporal intensity) are shown at two distances from a sinusoidal phase screen with a 450- μm period. The simulations show clear evidence of phase-to-amplitude conversion after propagation over 1 m. The resulting satellite pulses, however, are qualitatively similar in magnitude and temporal location.

This conclusion is reinforced in Fig. 127.19, which shows results from numeric simulations that included scalar Fresnel propagation between two Lorentzian phase screens. The distance between them was varied and the far-field intensity in the u - t plane was calculated. In one case, shown in Fig. 127.19(a), the two Lorentzian phase screens were coincident. In Fig. 127.19(b), the screens were separated by 1 m. Differences can be seen in the fine-scale structure, but the average far-field intensity is very similar, even though the separation between phase screens is orders of magnitude more than the coherence length, $l_c = 100 \mu\text{m}$, and the beam size, $W = 1 \text{ mm}$.

For the remainder of this article, therefore, diffraction is not included when estimating the nature of temporal contrast degradation for standard stretcher and compressor designs. Instead, the contributions from each phase screen are added according to Eq. (26).

2. Grating-Based Pulse Compressor and Öffner Stretcher

A schematic of a standard four-grating compressor is shown in Fig. 127.20(a). The gratings, G_1 and G_2 , in the first pair geometrically disperse the input pulse into its spectral components, which are recombined by the second pair. The group delay through the compressor for each component decreases approximately linearly with frequency, corresponding to negative dispersion.^{2,16} The magnitude of dispersion depends on the slant distances between the gratings in each pair, which are usually, but not always, matched.¹⁷ The compressor produces short pulses by compensating for the residual positive dispersion of the stretcher and amplifier glass.

Nonuniformity in the optical surfaces of G_2 and G_3 imprints onto the spectral phase of the pulse. The two gratings can be modeled as perfect elements plus additional phase screens. A retroreflector, placed at the AA' plane to halve the number of required gratings, can potentially degrade the temporal contrast and would be treated as a third phase screen.

A simulation of the output far-field intensity is shown in Fig. 127.20(b). The PSD parameters for the gratings were chosen arbitrarily according to Table 127.I. In this device, the

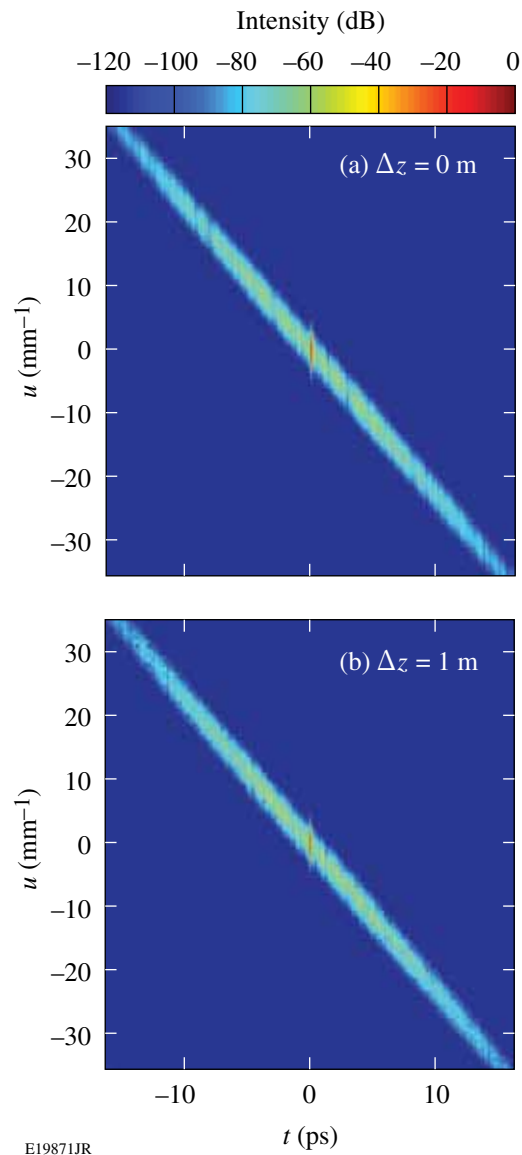
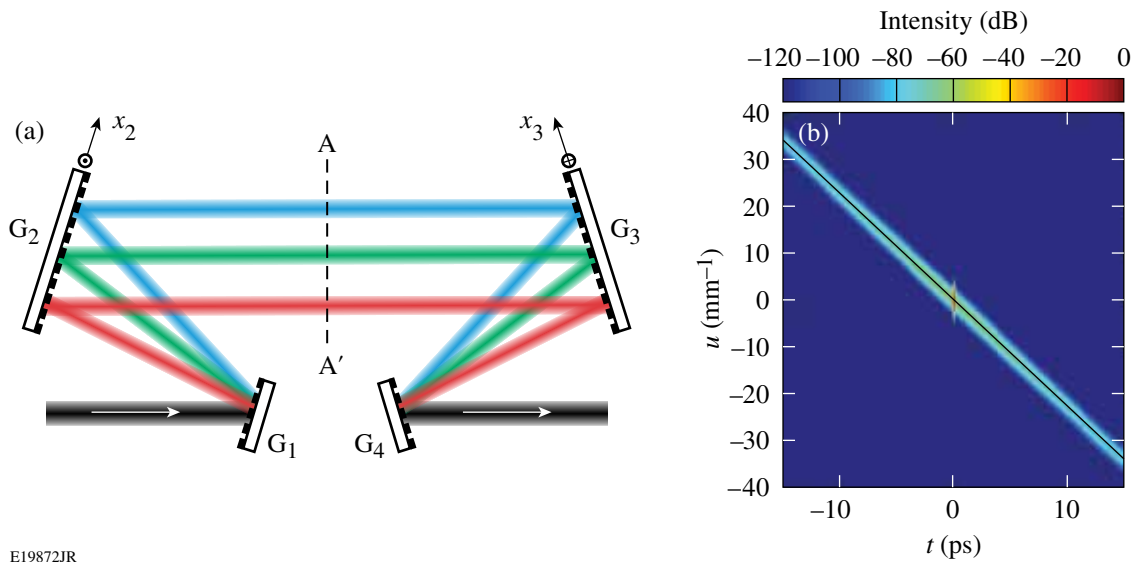


Figure 127.19

Far-field intensity calculated in the u - t plane for two phase screens. (a) Simulation results where phase screens were coincident, and (b) simulation results where phase screens were separated by $\Delta z = 1 \text{ m}$. Each spectral field after the first phase screens was propagated to the second using a scalar Fresnel propagation code. The details of the intensity structure between (a) and (b) are different, but any differences between the average profiles are insignificant.

two phase screens have the same spatio-spectral coefficient, $y = 0.44 \text{ mm/THz}$, and therefore the noise contributions from each grating follow the same line $u = -t/\gamma$.

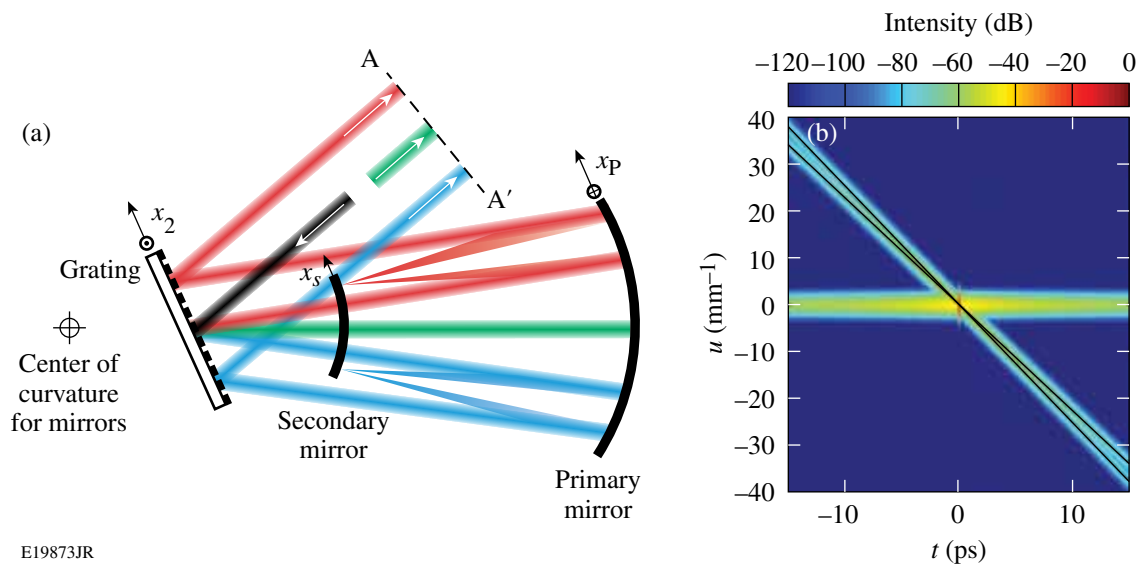
The far-field intensity distribution for an Öffner stretcher is qualitatively different (see Fig. 127.21). In this device, positive dispersion is obtained using a primary and secondary mir-



E19872JR

Figure 127.20

(a) Schematic of a four-grating compressor, showing the input and output beams (black) and three spectral components. Modulation on the surfaces of G_2 and G_3 produces spectral phase noise. A roof mirror can be used along the line AA' to retroreflect the beam, halving the required number of gratings. (b) Far-field average intensity calculated using Lorentzian PSD's in the $u-t$ plane at $t = 0$. G_2 and G_3 have the same spatio-spectral coefficient, $\gamma = 0.44$ mm/THz. The black line corresponds to $u = -t/\gamma$ and tracks the peak intensity from the PSD term.



E19873JR

Figure 127.21

(a) Schematic of an Öffner stretcher, showing the input beam (black) and three spectral components. (b) Far-field average intensity calculated using the same Lorentzian PSD for each optic in the $u-t$ plane at $t = 0$.

ror to form an image of a single grating, thereby achieving a negative separation distance.¹³ Modulation on the surfaces of the grating and primary and secondary mirrors produces spectral phase noise. A roof mirror (not shown) is typically used along the line AA' to retroreflect the beam at a different height back through the stretcher, eliminating spatial chirp. In

this simulation, the spatio-spectral coefficients γ are 0.44, 0.22, and 0.40 mm/THz for the primary mirror, secondary mirror, and grating, respectively.

The secondary mirror is located at a focal plane for each spectral component so, therefore, phase noise added to each

component is transferred directly to the system's far field. The resulting pedestal is centered on the main focal spot (at $u = v = 0$) and can be calculated using Eq. (13), but with spatial coordinates (x', y') replaced with angular coordinates (u, v) , where $u = kx/f$. The primary mirror and grating are located in the near-field planes, however, and therefore the pedestals that they produce are swept across the focal spot, as predicted by Eq. (10).

When identical PSD's are assumed for all optics, the secondary mirror has the largest impact on the contrast degradation. This is fundamentally different than on a compressor, where the surface quality of all optics in the spectrally dispersed planes affects the contrast equally.

Conclusions

A theoretical study was presented on the impact of high-frequency spectral phase modulation on the temporal contrast of ultrafast pulses. Expressions were derived for the intensity pedestal produced by optical surface roughness of components within pulse stretchers and compressors. The average intensity in the far field—the target location for ultra-intense experiments—was evaluated. Analytic closed-form expressions show that spectral phase imprint in the near field of a spectrally dispersed beam produces space–time coupling in the far field. As a result, the low-intensity pedestal that precedes the peak of the pulse sweeps across the target, covering an area many times the diffraction-limited spot size. Simulations of standard stretcher and compressor designs show fundamentally different forms of temporal contrast degradation at focus. These observations raise interesting questions about the nature of the target interaction when such impairments are present and about the validity of applying measurements made in the near field (the usual domain for high-dynamic-range cross-correlators¹⁸) to the target plane.

ACKNOWLEDGMENT

This work has been supported by the U.S. Department of Energy Office of Inertial Confinement Fusion under Cooperative Agreement No. DE-FC52-08NA28302, the University of Rochester, and the New York State Energy Research and Development Authority. The support of DOE does not constitute an endorsement by DOE of the views expressed in this article.

Appendix A

Equation (10) is obtained from Eq. (9) by first replacing variable pairs such as x and x' with X and Δx , where $X = x + x'$ and $\Delta x = x - x'$. The Jacobian of each transformation is 1/2. Equation (9) is then written as

$$\begin{aligned} \langle I(u, v, t) \rangle &= I_0(u, v, t) \\ &+ \frac{1}{2^3} \int_{-\infty}^{\infty} \dots \int_{-\infty}^{\infty} d\Omega d\Delta\omega dX d\Delta x dY d\Delta y \\ &\times \tilde{E}_0\left(\frac{X + \Delta x}{2}, \frac{Y + \Delta y}{2}, \frac{\Omega + \Delta\omega}{2}\right) \\ &\times \tilde{E}_0^*\left(\frac{X - \Delta x}{2}, \frac{Y - \Delta y}{2}, \frac{\Omega - \Delta\omega}{2}\right) \\ &\times C(\Delta x - \gamma\Delta\omega, \Delta y) e^{-i\Delta\omega t} e^{-i\Delta x u} e^{-i\Delta y v}, \end{aligned} \quad (27)$$

where the phase map has been assumed to be wide-sense stationary, so that

$$C(\Delta x, \Delta y) = \langle \phi(x, y) \phi^*(x', y') \rangle. \quad (28)$$

The integrals over Ω , X , and Y involve only the spectral near fields \tilde{E}_0 and not the correlation function. Replacing these fields with their temporal Fourier transforms adds integrals over t' and t'' to give a portion of the integrand of Eq. (27) that is

$$\begin{aligned} \int_{-\infty}^{\infty} \dots \int_{-\infty}^{\infty} d\Omega dX dY dt' dt'' E_0\left(\frac{X + \Delta x}{2}, \frac{Y + \Delta y}{2}, t'\right) \\ \times E_0^*\left(\frac{X - \Delta x}{2}, \frac{Y - \Delta y}{2}, t''\right) \\ \times e^{i\left(\frac{\Omega + \Delta\omega}{2}\right)t'} e^{-i\left(\frac{\Omega - \Delta\omega}{2}\right)t''}. \end{aligned} \quad (29)$$

Collecting exponential factors that depend only on Ω and completing the integral gives a Dirac delta function $2\delta(t' - t'')$. This allows one to evaluate the t'' integral, giving

$$\begin{aligned} 2 \int_{-\infty}^{\infty} \dots \int_{-\infty}^{\infty} dX dY dt' E_0\left(\frac{X + \Delta x}{2}, \frac{Y + \Delta y}{2}, t'\right) \\ \times E_0^*\left(\frac{X - \Delta x}{2}, \frac{Y - \Delta y}{2}, t'\right) e^{i\Delta\omega t'}. \end{aligned} \quad (30)$$

That is, each field in Eq. (27) is replaced by its temporal Fourier transform, the integral over Ω is replaced by an integral over its conjugate variable, and a phase factor of $2e^{i\Delta\omega t'}$ is added. Repeating this operation for the integrals over X and Y gives the following equivalent expression for Eq. (29):

$$2^3 \int_{-\infty}^{\infty} \dots \int_{-\infty}^{\infty} dt' du' dv' I_0(u', v', t') e^{i\Delta\omega t'} e^{i\Delta x u'} e^{i\Delta y v'}. \quad (31)$$

Equation (27) is therefore rewritten as

$$\begin{aligned} \langle I(u, v, t) \rangle &= I_0(u, v, t) \\ &+ \int_{-\infty}^{\infty} \dots \int_{-\infty}^{\infty} du' dv' dt' d\Delta\omega d\Delta x d\Delta y I_0(u', v', t') \\ &\times C(\Delta x - \gamma\Delta\omega, \Delta y) \\ &\times e^{-i\Delta\omega(t-t')} e^{-i\Delta x(u-u')} e^{-i\Delta y(v-v')}. \end{aligned} \quad (32)$$

The integrals over Δx and Δy are Fourier transforms of the correlation function, which is equal to the power spectral density of the phase screen and is defined as

$$\text{PSD}(u, v) = \int_{-\infty}^{\infty} d\Delta x d\Delta y C(\Delta x, \Delta y) e^{-i\Delta x u} e^{-i\Delta y v}, \quad (33)$$

The remaining integral over $\Delta\omega$ is evaluated to give the Dirac delta function $\delta(t - t' + \gamma u - \gamma v)$. This makes it possible to complete the integral over t' , which gives

$$\begin{aligned} \langle I(u, v, t) \rangle &= I_0(u, v, t) \\ &+ \int_{-\infty}^{\infty} \int_{-\infty}^{\infty} du' dv' I_0(u', v', t' + \gamma u - \gamma v) \\ &\times \text{PSD}(u - u', v - v'). \end{aligned} \quad (34)$$

Appendix B

Equation (14) is obtained by first integrating the 2-D PSD function over v , the axis normal to the plane of geometric dispersion:

$$\begin{aligned} &\int_{-\infty}^{\infty} \text{PSD}(u, v) dv \\ &= \int_{-\infty}^{\infty} \int_{-\infty}^{\infty} d\Delta x d\Delta y C(\Delta x, \Delta y) e^{-i\Delta x u} \left(\int_{-\infty}^{\infty} dv e^{-i\Delta y v} \right). \end{aligned} \quad (35)$$

The quantity in parentheses is equal to $\delta(\Delta y)$, making it possible for the integral over Δy to complete. Finally, by noting

that $C(-\gamma\Delta\omega, 0) = C_{xy}(\Delta\omega)$, making the substitutions $\Delta x = \gamma\Delta\omega$ and $u = t/\gamma$, and using the fact that

$$\text{PSD}_{xy}(t) = \int_{-\infty}^{\infty} d\Delta\omega C_{xy}(\Delta\omega) e^{-i\Delta\omega t},$$

one obtains the connection between the two PSD functions:

$$\int_{-\infty}^{\infty} dv \text{PSD}(t/\gamma, v) = \gamma \text{PSD}_{xy}(t). \quad (36)$$

REFERENCES

1. P. Maine *et al.*, IEEE J. Quantum Electron. **24**, 398 (1988).
2. E. B. Treacy, IEEE J. Quantum Electron. **QE-5**, 454 (1969).
3. A. Antonetti *et al.*, Appl. Phys. B **65**, 197 (1997).
4. V. Bagnoud and F. Salin, J. Opt. Soc. Am. B **16**, 188 (1999).
5. K.-H. Hong *et al.*, Appl. Phys. B **81**, 447 (2005).
6. C. Hooker *et al.*, Opt. Express **19**, 2193 (2011).
7. J. W. Goodman, *Statistical Optics*, Wiley Series in Pure and Applied Optics (Wiley, New York, 1985).
8. C. Dorrer and J. Bromage, Opt. Express **16**, 3058 (2008).
9. M. M. Wefers and K. A. Nelson, IEEE J. Quantum Electron. **32**, 161 (1996).
10. E. Sidick, in *Modeling Aspects in Optical Metrology II*, edited by H. Bosse, B. Bodermann, and R. M. Silver (SPIE, Bellingham, WA, 2009), Vol. 7390, p. 73900L.
11. J. C. Dainty, J. Opt. Soc. Am. **62**, 595 (1972).
12. E. L. Church, P. Z. Takacs, and T. A. Leonard, in *Scatter from Optical Components*, edited by J. C. Stover (SPIE, Bellingham, WA, 1990), Vol. 1165, pp. 136–150.
13. G. Chériaux *et al.*, Opt. Lett. **21**, 414 (1996).
14. H. F. Talbot, Lond. & Edin. Phil. Mag. & J. of Sci., Third Series **9**, 401 (1836).
15. P. Latimer and R. F. Crouse, Appl. Opt. **31**, 80 (1992).
16. I. Walmsley, L. Waxer, and C. Dorrer, Rev. Sci. Instrum. **72**, 1 (2001).
17. H. Huang and T. J. Kessler, Opt. Lett. **32**, 1854 (2007).
18. S. Luan *et al.*, Meas. Sci. Technol. **4**, 1426 (1993).

Highly Accurate Wavefront Reconstruction Algorithms Over Broad Spatial-Frequency Bandwidth

Introduction

Frequency-domain wavefront reconstruction methods are as old as the very early wavefront reconstructors.^{1,2} Freischlad placed this subject on solid ground.³ The rectangular map constraint of the conventional Fourier method has been removed in an iterative Gerchberg-type algorithm dealing with an arbitrary boundary shape.⁴ A series of recent papers by Poyneer discuss improvements on handling boundary conditions and applications in extreme adaptive optics.^{5,6} Similar principles have been applied in shearing interferometers.⁷ More serious attention has been paid to the accuracy of the reconstruction methods in Refs. 8–10. The works of Campos and Yaroslavsky presented a solution based on a band-limited integration technique in frequency domain. The two-dimensional (2-D) extension of the same method was not discussed. Complementary to their works, Bahk introduced a full 2-D wavefront reconstructor based on the band-limited derivative calculation.¹¹ Both approaches emphasize the frequency response of the reconstructed signals. The frequency response of wavefront reconstruction has been discussed earlier in the analysis of lateral-shearing interferometry.¹² Frequency-response characteristics of a reconstruction is important in focal-spot diagnostics for high-power lasers, where the focal spot is indirectly characterized using wavefront information reconstructed from Shack–Hartmann slopes data.¹³

This article develops a set of encompassing mathematical tools for wavefront reconstruction problems, where many additional benefits naturally arise, interconnecting the results of previous works. The benefits are exemplified by the development of two new wavefront reconstructors and the analytical derivation of noise-propagation coefficients of several well-known wavefront reconstructors.

This article is organized as follows: (1) The mathematical tools and symbols regarding band-limited derivative operations, which are needed for the analyses in the subsequent sections, are introduced. (2) A way to improve the accuracy of the finite-difference method is discussed in connection with wavefront reconstruction. The Simpson rule is adopted for developing a

new spatial-domain iterative reconstruction algorithm. The exact details of the algorithm and its frequency-domain property are described. (3) A band-limited reconstruction algorithm is extended to hexagonal geometry, which greatly enhances the flexibility of band-limited reconstructors. (4) Finally, the noise-propagation curve is analytically derived and compared with numerical simulations.

Band-Limited Derivative

The main results of band-limited derivative techniques in the context of wavefront reconstruction were summarized in Ref. 11. The full derivation of the results will be presented here for the sake of completeness. Additional new notations are introduced that will simplify the expressions in **Hexagonal Band-Limited Reconstructor** (p. 136).

The motivation for band-limited derivatives, especially for discrete samples, lies in the fact that it provides an analytical tool for converting back and forth between slope measurements and wavefront signal. We start by asking what the exact interpolation formula is for derivatives in discrete samples. According to sampling theorem, a band-limited signal can be exactly reconstructed at any point by convolving a sinc function with discrete samples. The derivative of a band-limited signal is obtained by directly differentiating the sinc function's convolution kernel that becomes a spherical Bessel function (j_1) (Ref. 14). The derivative interpolation expression at discrete points is

$$\begin{aligned} \frac{d\varphi}{dx} \Big|_{(x = m\Delta x)} &\equiv \varphi_x(m) \\ &= \frac{1}{\Delta x} \sum_{n=1}^{\infty} \pi j_1(n\pi) \left\{ \varphi[(m+n)\Delta x] - \varphi[(m-n)\Delta x] \right\}, \quad (1) \end{aligned}$$

where the spherical Bessel function evaluated at integer multiples of π is equivalent to

$$\pi j_1(n\pi) = \frac{(-1)^{n+1}}{n}, \quad n = 1, 2, \dots \quad (2)$$

The summation of the left-hand side of Eq. (1) for all sample points can be shown to be equal to zero by taking advantage of the expression on the right-hand side and using the periodicity condition of discrete samples:

$$\sum_{m=0}^{N-1} \frac{d\varphi}{dx} \Big|_{(x=m\Delta x)} = 0. \quad (3)$$

Equation (1) is easier to handle in frequency domain. Discrete Fourier transform (DFT) and Fourier series analysis lead to the following equivalent expression:

$$\overline{\varphi}_x(k) = i \frac{2\pi}{\Delta x} \mathfrak{S}(k) \tilde{\varphi}(k), \quad (4)$$

where the tilde notation means DFT of the symbol beneath it and $\mathfrak{S}(k)$ (sawtooth wave) is defined as

$$\mathfrak{S}(k) = \begin{cases} \text{for even } N \begin{cases} \frac{k}{N}, & k = 0, \dots, N/2 - 1 \\ 0, & k = N/2 \\ \frac{k}{N} - 1, & k = \frac{N}{2} + 1, \dots, N - 1 \end{cases} \\ \text{for odd } N \begin{cases} \frac{k}{N}, & k = 0, \dots, (N-1)/2 \\ \frac{k}{N} - 1, & k = (N+1)/2, \dots, N - 1 \end{cases} \end{cases} \quad (5)$$

Equation (4) provides a convenient way of calculating exact derivatives from band-limited signals. When the sampling points of a derivative signal are offset by a half-sampling space from the sampling points of the original signal, a slightly different form should be used:

$$\begin{aligned} \frac{d\varphi}{dx} \Big|_{(x=m\Delta x + \frac{1}{2}\Delta x)} &\equiv \varphi_{x,1/2}(m) \\ &= \frac{1}{\Delta x} \sum_{n=1}^{\infty} \pi j_1 \left(n\pi - \frac{1}{2}\pi \right) \\ &\quad \times \left\{ \varphi[(m+n)\Delta x] - \varphi[(m-n+1)\Delta x] \right\}, \end{aligned} \quad (6)$$

where the Bessel coefficients can be replaced again with an integral expression

$$\pi j_1 \left(n\pi - \frac{1}{2}\pi \right) = \frac{4}{\pi} \frac{(-1)^{n+1}}{(2n-1)^2}, \quad n = 1, 2, \dots \quad (7)$$

Employing a similar Fourier series analysis that leads to Eq. (4), the frequency-domain expression of Eq. (6) is reduced to

$$\overline{\varphi}_{x,1/2}(k) = i \frac{2\pi}{\Delta x} \exp\left(i \frac{\pi}{N} k\right) \mathfrak{T}(k) \tilde{\varphi}(k), \quad (8)$$

where $\mathfrak{T}(k)$ (triangular wave) is defined as

$$\mathfrak{T}(k) = \begin{cases} k/N, & k = 0, \dots, \left\lfloor \frac{N-1}{2} \right\rfloor \\ 1 - k/N, & k = \left\lfloor \frac{N-1}{2} \right\rfloor + 1, \dots, N-1 \end{cases} \quad (9)$$

We also need an interpolation formula for creating a signal shifted by half-sample spacing for Fried geometry:

$$\begin{aligned} \varphi(x) \Big|_{(x=m\Delta x + \frac{1}{2}\Delta x)} &\equiv \varphi_{1/2}(m) \\ &= \sum_{n=1}^{\infty} \text{sinc}\left(n - \frac{1}{2}\right) \left\{ \varphi[(m+n)\Delta x] - \varphi[(m-n+1)\Delta x] \right\}. \end{aligned} \quad (10)$$

The DFT of Eq. (10) is

$$\overline{\varphi}_{1/2}(k) = \exp\left(i \frac{\pi}{N} k\right) \mathfrak{R}(k) \tilde{\varphi}(k), \quad (11)$$

where $\mathfrak{R}(k)$ (rectangular wave) is

$$\mathfrak{R}(k) = \begin{cases} \text{for even } N \begin{cases} 1, & k = 0, \dots, N/2 - 1 \\ 0, & k = N/2 \\ -1, & k = N/2 + 1, \dots, N - 1 \end{cases} \\ \text{for odd } N \begin{cases} 1, & k = 0, \dots, (N-1)/2 \\ -1, & k = (N+1)/2, \dots, N - 1 \end{cases} \end{cases} \quad (12)$$

Therefore, the partial derivative in the x direction for Fried geometry in frequency domain is

$$\begin{aligned} \overline{\varphi}_{x,1/2,1/2}(p,q) \\ = i \frac{2\pi}{\Delta x} \exp\left[i \frac{\pi}{N} (p+q)\right] \mathfrak{T}(q) \mathfrak{R}(p) \tilde{\varphi}(p,q). \end{aligned} \quad (13)$$

Equation (13) has an additional degree of freedom (index p for the y direction) because the reconstructed sample point in the Fried geometry must first be shifted in the y direction by a half-sample size before applying the half-sample shifted-derivative operation in the x direction.

For consistency, we can verify that the sequential operations of half-pixel shift and derivative operation using $\mathbb{R}(k)$ and $\mathbb{S}(k)$ produce the same result as single operation of $\mathbb{T}(k)$, i.e., $\mathbb{T}(k) = \mathbb{R}(k)\mathbb{S}(k)$. This relation, however, does not hold for the value at $N/2$ for even N , where the left-hand side is 0.5, whereas the right-hand side is 0. To remove this paradox for an even number of samples, we choose to use $\mathbb{S}(N/2) = 0.5$ and $\mathbb{R}(N/2) = 1$ or $\mathbb{S}(N/2) = -0.5$ and $\mathbb{R}(N/2) = -1$. A similar choice was made in Ref. 9 for band-limited integration operators from a different perspective. *The redefinition of \mathbb{S} and \mathbb{R} at the midpoint is implied from hereon.* Using the new definition, the half-pixel operator used in the right-hand side of Eq. (11) can be alternatively expressed as

$$\exp\left(\pm \frac{\pi i}{N} k\right) \mathbb{R}(k) = \exp[\pm \pi i \mathbb{S}(k)]. \quad (14)$$

We can establish the connection from discrete to continuous variable derivative as follows: \mathbb{S} can be considered as a discrete angular frequency vector circularly shifted by $[N/2]$. If we define $k_x(p) = (2\pi/\Delta x)p$ for $p = 0, \dots, (N-1)$, then

$$\frac{2\pi}{\Delta x} \mathbb{S} = \overline{k_x}, \quad (15)$$

where the bar over k_x denotes a circular shift by $[N/2]$. Using Eq. (14), Eqs. (4), (8), and (11) can be alternatively expressed as

$$\overline{\varphi_x} = i \overline{k_x} \tilde{\varphi}, \quad (16)$$

$$\overline{\varphi_{x,1/2}} = i \overline{k_x} \exp\left(i \frac{\Delta x}{2} \overline{k_x}\right) \tilde{\varphi}, \quad (17)$$

$$\overline{\varphi_{1/2}} = \exp\left(i \frac{\Delta x}{2} \overline{k_x}\right) \tilde{\varphi}, \quad (18)$$

The $\overline{k_x}$ notation establishes the formal connection with continuous variable derivatives.

In many practical situations, the band-limited calculations may not produce exact results, depending on the nature of signals. The magnitudes of the Fourier coefficients of a linear function, for example, decrease as $1/(\text{spatial frequency})$, whereas Eq. (16) indicates that the coefficients of the derivative are multiplied by the spatial-frequency vector. Therefore, the highest spatial-frequency coefficient does not vanish, even if N approaches ∞ . Therefore, the linear terms are not band limited and need to be treated separately. Equations (16)–(18) form the basis of the following analysis.

Simpson Reconstructor

The analysis in the previous section suggests that an accurate derivative calculation at discrete samples requires the superposition sum of the whole set of samples. This can be done more conveniently in the frequency domain, which results in a band-limited reconstructor with unity frequency response.¹¹ On the other hand, it is still worthwhile to investigate an improved finite-difference scheme for purely spatial-domain operation. In finite-difference methods involving only a few points, a high degree of accuracy is preserved by distributing the finite difference over both the measured derivative samples (i.e., slopes) and the integrated samples. Denoting the wavefront estimate as $\hat{\varphi}$ and the measured slope as S , one can start from a general finite-difference expression such as

$$\sum_j a(j) \hat{\varphi}(i+j) = \sum_k b(k) S(i+k) \quad (19)$$

for 1-D problems. Coefficients a and b belong to a specific finite-difference scheme. For example, Southwell¹⁴ showed a reconstructor based on

$$\hat{\varphi}(i+1) - \hat{\varphi}(i) = \frac{\Delta x}{2} [S(i) + S(i+1)]. \quad (20)$$

The frequency response of the Southwell reconstructor is low at high spatial frequency. We enhance the frequency response using the Simpson rule, which is

$$\hat{\varphi}(i+1) - \hat{\varphi}(i-1) = \frac{\Delta x}{3} [S(i-1) + 4S(i) + S(i+1)]. \quad (21)$$

An iterative wavefront reconstruction based on this scheme will be developed in the next section.

1. Simpson Iterator

Casting the local 1-D Eq. (21) into a least squares form in 2-D, we obtain an error metric (ε) as

$$\begin{aligned} \varepsilon = \sum_{i,j} & \left\{ \frac{1}{2\Delta x} [\hat{\varphi}(i,j+1) - \hat{\varphi}(i,j-1)] \right. \\ & \left. - \frac{1}{6} [S_x(i,j+1) + 4S_x(i,j) + S_x(i,j-1)] \right\}^2 \\ & + \left\{ \frac{1}{2\Delta y} [\hat{\varphi}(i+1,j) - \hat{\varphi}(i-1,j)] \right. \\ & \left. - \frac{1}{6} [S_y(i+1,j) + 4S_y(i,j) + S_y(i-1,j)] \right\}^2. \quad (22) \end{aligned}$$

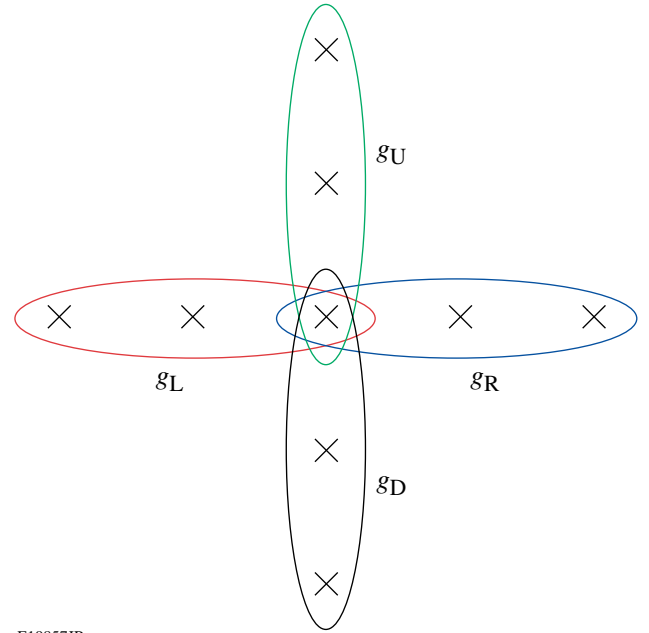
Δx and Δy are moved around to the $\hat{\phi}$ side so that squared terms are in units of slopes. This provides equal weight to the differences in x and y directions on the assumption that the magnitude of slopes is comparable in either direction.

The condition $\partial \varepsilon / \partial \hat{\phi}(i, j) = 0$ leads to an equation that can be used for the iterative algorithm. It is assumed that phase and slope points are embedded in an arbitrary region. The differentiation of the error metric results in four groups, which are indicated by different colors in Fig. 127.22. Each group can be used in the equation only when all of its elements exist. This strategy is realized by using g parameters as shown in the following:

SIMPSON:

$$\begin{aligned}
 & g_L [\hat{\phi}(i, j) - \hat{\phi}(i, j - 2)] + g_R [\hat{\phi}(i, j) - \hat{\phi}(i, j + 2)] \\
 & + g_U \left(\frac{\Delta x}{\Delta y} \right)^2 [\hat{\phi}(i, j) - \hat{\phi}(i - 2, j)] \\
 & + g_D \left(\frac{\Delta x}{\Delta y} \right)^2 [\hat{\phi}(i, j) - \hat{\phi}(i + 2, j)] \\
 = & g_L [S_x(i, j - 2) + 4S_x(i, j - 1) + S_x(i, j)] \frac{\Delta x}{3} \\
 & - g_R [S_x(i, j) + 4S_x(i, j + 1) + S_x(i, j + 2)] \frac{\Delta x}{3} \\
 & + g_U \left(\frac{\Delta x}{\Delta y} \right)^2 [S_y(i - 2, j) + 4S_y(i - 1, j) + S_y(i, j)] \frac{\Delta y}{3} \\
 & - g_D \left(\frac{\Delta x}{\Delta y} \right)^2 [S_y(i, j) + 4S_y(i + 1, j) + S_y(i + 2, j)] \frac{\Delta y}{3} \\
 \equiv & \Delta S(i, j). \tag{23}
 \end{aligned}$$

g_L , g_R , g_U , and g_D are flags with values 0 or 1, where L, R, U, and D indicate left, right, up, and down directions, respectively. They are 0's if the quantities in the parentheses next to them are incalculable or 1's otherwise. For example, g_L at the point (i, j) does not vanish only when the slopes' measurements exist at the additional points at $(i, j - 1)$ and $(i, j - 2)$. The scope of each flag is graphically indicated in Fig. 127.22. For comparison, the iterative equation for the Southwell reconstructor is written here using the same format.



E19857JR

Figure 127.22
Simpson iterator geometry.

SOUTHWELL:

$$\begin{aligned}
 & g_L [\hat{\phi}(i, j) - \hat{\phi}(i, j - 1)] + g_R [\hat{\phi}(i, j) - \hat{\phi}(i, j + 1)] \\
 & + g_U \left(\frac{\Delta x}{\Delta y} \right)^2 [\hat{\phi}(i, j) - \hat{\phi}(i - 1, j)] \\
 & + g_D \left(\frac{\Delta x}{\Delta y} \right)^2 [\hat{\phi}(i, j) - \hat{\phi}(i + 1, j)] \\
 = & g_L [S_x(i, j - 1) + S_x(i, j)] \frac{\Delta x}{2} \\
 & - g_R [S_x(i, j) + S_x(i, j + 1)] \frac{\Delta x}{2} \\
 & + g_U \left(\frac{\Delta x}{\Delta y} \right)^2 [S_y(i - 1, j) + S_y(i, j)] \frac{\Delta y}{2} \\
 & - g_D \left(\frac{\Delta x}{\Delta y} \right)^2 [S_y(i, j) + S_y(i + 1, j)] \frac{\Delta y}{2}. \tag{24}
 \end{aligned}$$

The same successive-over-relaxation technique¹⁵ can be applied to the Simpson iterative reconstructor:

$$\hat{\phi}^{(m+1)}(i, j) = \hat{\phi}^{(m)}(i, j) + \omega \left[\overline{\hat{\phi}^{(m)}}(i, j) - \hat{\phi}^{(m)}(i, j) \right], \tag{25}$$

where

$$\begin{aligned} & \overline{\hat{\phi}^{(m)}}(i,j) \\ &= \left[\overline{\hat{\phi}_0^{(m)}}(i,j) + \Delta S(i,j) \right] / (g_L + g_R + g'_U + g'_D), \end{aligned} \quad (26)$$

$$\begin{aligned} \overline{\hat{\phi}_0^{(m)}}(i,j) &= g_L \hat{\phi}^{(m)}(i,j-2) \\ &+ g_R \hat{\phi}^{(m)}(i,j+2) + g'_U \hat{\phi}^{(m)}(i-2,j) \\ &+ g'_D \hat{\phi}^{(m)}(i+2,j). \end{aligned} \quad (27)$$

Here, ω is the over-relaxation parameter; g' is $(\Delta x/\Delta y)^2 \cdot g$.

2. Frequency Response and Regularization

The frequency response of the Simpson reconstructor will be calculated following the method presented in Ref. 11. The sum of the squared error in the spatial domain in Eq. (22) is equivalent to the sum of the squared error of the Fourier-transformed component by the Parseval theorem:

$$\varepsilon = \frac{1}{N^2} \sum \left\{ \left| D_x \tilde{\phi} - A_x \tilde{S}_x \right|^2 + \left| D_y \tilde{\phi} - A_y \tilde{S}_y \right|^2 \right\}, \quad (28)$$

where

$$D_x = \frac{1}{2\Delta x} \left[\exp(i\bar{k}_x \Delta x) - \exp(-i\bar{k}_x \Delta x) \right] \equiv D_{x,\text{Simpson}} \quad (29)$$

and

$$A_x = \frac{1}{6} \left[\exp(i\bar{k}_x \Delta x) + 4 + \exp(-i\bar{k}_x \Delta x) \right] \equiv A_{x,\text{Simpson}}. \quad (30)$$

The solution for $\tilde{\phi}$ in Eq. (28) is

$$\tilde{\phi} = \frac{(D_x^* A_x \tilde{S}_x + D_y^* A_y \tilde{S}_y)}{|D_x|^2 + |D_y|^2}. \quad (31)$$

As $\tilde{S}_x = i\bar{k}_x \tilde{\phi}$ and $\tilde{S}_y = i\bar{k}_y \tilde{\phi}$, the frequency response H defined as the ratio of the reconstructed wavefront amplitude to the true wavefront amplitude associated with the measured slopes at a given spatial frequency point is

$$H = \frac{\tilde{\phi}}{\hat{\phi}} = \frac{(D_x^* A_x D_{x,0} + D_y^* A_y D_{y,0})}{|D_x|^2 + |D_y|^2}, \quad (32)$$

where new notations $D_{x,0}$ and $D_{y,0}$ were introduced in place of $i\bar{k}_x$ and $i\bar{k}_y$, respectively.

Applying the Simpson derivative and average operators [Eqs. (29) and (30)], we obtain

$$\begin{aligned} & H_{\text{Simpson}} \\ &= \frac{1}{3} \frac{\omega_x \sin \omega_x (2 + \cos \omega_x) + \omega_y \sin \omega_y (2 + \cos \omega_y)}{\sin^2 \omega_x + \sin^2 \omega_y}, \end{aligned} \quad (33)$$

where $\bar{k}_x \Delta x \equiv \omega_x = 2\pi f_x$ and $\bar{k}_y \Delta x \equiv \omega_y = 2\pi f_y$, f_x and f_y are normalized frequencies ranging from -0.5 to 0.5 . It is assumed $\Delta x = \Delta y$. The frequency response of H_{Simpson} has eight singularities on the four corners and side centers. Except for the region near the poles, the frequency response is nearly unity everywhere, which proves higher accuracy of the Simpson rule than the traditional reconstructors over all spectrums in wavefront reconstruction (refer to Fig. 1 of Ref. 11).

The singularities can be removed by introducing the following Phillips regularization term¹⁶ to the right-hand side of Eq. (22):

$$\begin{aligned} \varepsilon_{\text{reg}} &= \lambda \sum_{i,j} \left\{ \frac{1}{(2\Delta x)^2} \left[\hat{\phi}(i,j+1) - 2\hat{\phi}(i,j) + \hat{\phi}(i,j-1) \right]^2 \right. \\ &\quad \left. + \frac{1}{(2\Delta y)^2} \left[\hat{\phi}(i+1,j) - 2\hat{\phi}(i,j) + \hat{\phi}(i-1,j) \right]^2 \right\}. \end{aligned} \quad (34)$$

In the frequency domain, this transforms into

$$\varepsilon_{\text{reg}} = \lambda \frac{1}{N^2} \sum \left\{ \left| D_{x,\text{reg}} \tilde{\phi} \right|^2 + \left| D_{y,\text{reg}} \tilde{\phi} \right|^2 \right\}, \quad (35)$$

where

$$D_{x,\text{reg}} = \frac{2}{\Delta x} \sin^2 \left(\frac{\bar{k}_x \Delta x}{2} \right), \quad (36)$$

and similarly for $D_{y,\text{reg}}$.

The denominator of the Simpson frequency response will have an additional term of $\lambda \left(|D_{x,\text{reg}}|^2 + |D_{y,\text{reg}}|^2 \right)$ that removes the singularity. The regularized frequency response is

$$\begin{aligned} & H_{\text{Simpson}}(\lambda) \\ &= \frac{1}{3} \frac{\omega_x \sin \omega_x (2 + \cos \omega_x) + \omega_y \sin \omega_y (2 + \cos \omega_y)}{\sin^2 \omega_x + \sin^2 \omega_y + 4\lambda \left(\sin^4 \frac{1}{2} \omega_x + \sin^4 \frac{1}{2} \omega_y \right)}. \end{aligned} \quad (37)$$

The 1-D frequency response with the regularization term has a second peak near high spatial frequency for sufficiently small λ (<0.08) [Fig. 127.23(b)]. The free parameter λ can be fixed to a value such that the second peak is 1. The numerically determined value of λ for such a condition is 0.07489. This choice of λ gives only a 3% error in wavefront amplitude over 80% of the frequency range. Another choice can be $\lambda = 0.07026$, which balances the local maximum and minimum around 1. The second option reduces the maximum deviation below 2.2% within 85% of the spectral range. Figure 127.23(a) shows a 3-D view of the frequency response of the Simpson-rule reconstructor with $\lambda = 0.07489$. The 1-D response is shown in Fig. 127.23(b). The solid line was calculated from an analytic expression [Eq. (36)], whereas the circles are from numerical simulations. The numerical simulation consists of steps of generating slopes from sinusoid wavefronts at a given spatial frequency and of reconstructing the wavefront and comparing the ratio between the original and the reconstructed wavefront amplitude at that frequency. The reconstruction algorithm used in the simulation will be explained in detail in the following section. The result shows good agreement with the analytic curve.

3. Iterative Algorithm with Regularization Terms

The frequency-domain analysis does not give a detailed picture of how the successive-over-relaxation method can be applied in spatial-domain iteration, especially around the measurement boundary. Resolving the stationary condition with the

regularization term gives additional terms on the left-hand side of Eq. (23). These are fully written out using g flags:

$$\begin{aligned}
 & (2\Delta x)^2 \frac{\partial \varepsilon_{\text{reg}}}{\partial \hat{\phi}(i,j)} \\
 &= \lambda g_L [\hat{\phi}(i,j) - 2\hat{\phi}(i,j-1) + \hat{\phi}(i,j-2)] \\
 &+ \lambda g_R [\hat{\phi}(i,j+2) - 2\hat{\phi}(i,j+1) + \hat{\phi}(i,j)] \\
 &+ \lambda g'_U [\hat{\phi}(i,j) - 2\hat{\phi}(i-1,j) + \hat{\phi}(i-2,j)] \\
 &+ \lambda g'_D [\hat{\phi}(i+2,j) - 2\hat{\phi}(i+1,j) + \hat{\phi}(i,j)] \\
 &- 2\lambda g'_{LR} [\hat{\phi}(i,j+1) - 2\hat{\phi}(i,j) + \hat{\phi}(i,j-1)] \\
 &- 2\lambda g'_{UD} [\hat{\phi}(i+1,j) - 2\hat{\phi}(i,j) + \hat{\phi}(i-1,j)]. \quad (38)
 \end{aligned}$$

g_{LR} or g_{UD} is 1 only if two points exist to the right and left or up and down, respectively, and zero otherwise. The iteration formula (26) will be modified to

$$\bar{\phi}(i,j) = \frac{[\bar{\phi}_0(i,j) + \Delta S(i,j) + \lambda \Delta \hat{\phi}(i,j)]}{[(1 + \lambda)(g_L + g_R + g'_U + g'_D) + 4\lambda(g_{LR} + g'_{UD})]}, \quad (39)$$

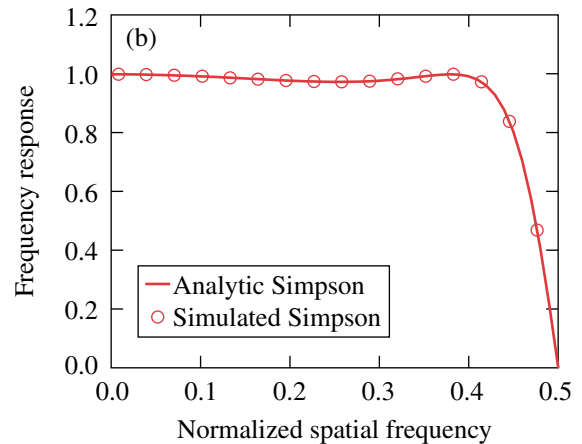
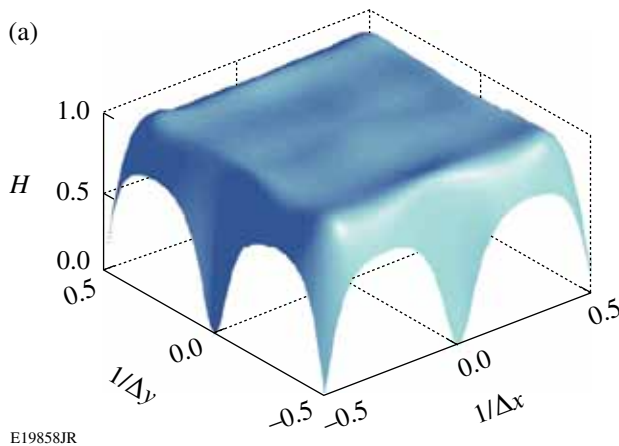


Figure 127.23

Frequency response of Simpson reconstructor with $\lambda = 0.07489$. (a) A 3-D view of the frequency response; (b) cross section along f_x axis. The solid line was calculated from the analytic expression; the circles are from simulations of Simpson iterator geometry.

where

$$\begin{aligned}
 \Delta\hat{\phi}(i,j) = & g_L [2\hat{\phi}(i,j-1) - \hat{\phi}(i,j-2)] \\
 & + g_R [2\hat{\phi}(i,j+1) - \hat{\phi}(i,j+2)] \\
 & + g'_U [2\hat{\phi}(i-1,j) - \hat{\phi}(i-2,j)] \\
 & + g'_D [2\hat{\phi}(i+1,j) - \hat{\phi}(i+2,j)] \\
 & + 2g_{LR} [\hat{\phi}(i,j+1) + \hat{\phi}(i,j-1)] \\
 & + 2g'_{UD} [\hat{\phi}(i+1,j) + \hat{\phi}(i-1,j)]. \quad (40)
 \end{aligned}$$

Hexagonal Band-Limited Reconstructor

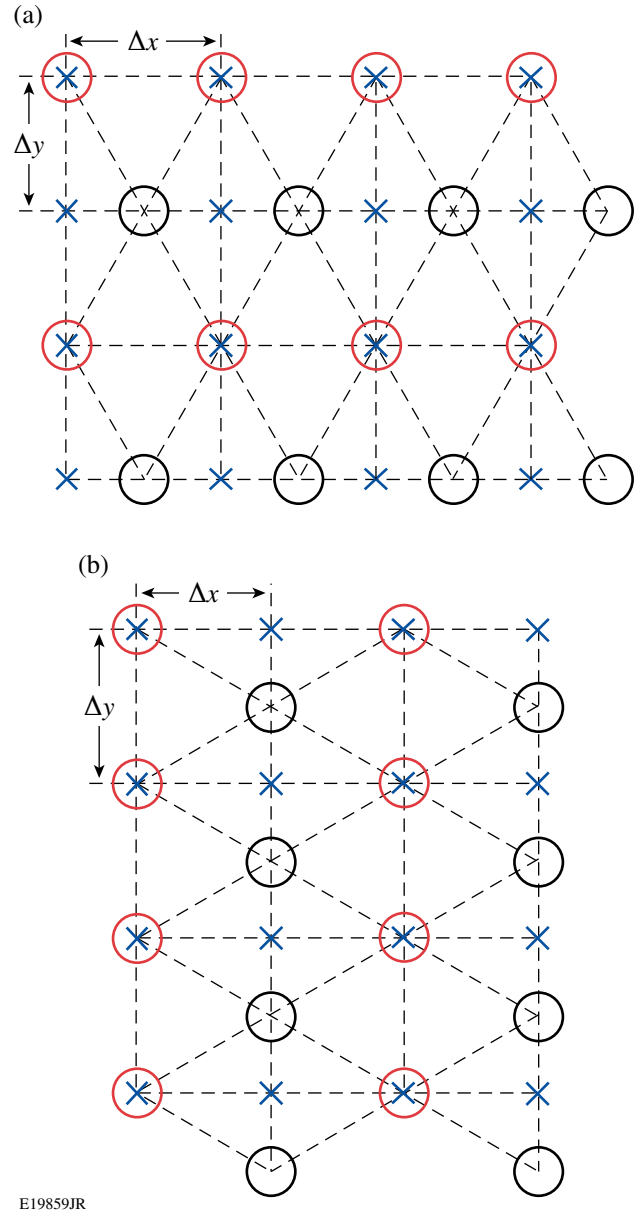
Band-limited reconstruction provides a unity frequency response over all spatial bandwidths. The band-limited reconstructor for the Southwell geometry was presented in Ref. 11. It was shown that band-limited derivative operators are also available for Hudgin and Fried geometries. Table 127.II summarizes the three operators depending on the geometry.

Table 127.II: Summary of band-limited derivative operators ($D_{x,0}$).

Geometry	$D_{x,0}$
Southwell	$i\bar{k}_x$
Hudgin	$i\bar{k}_x \exp[i\bar{k}_x(\Delta x/2)]$
Fried	$i\bar{k}_x \exp[i\bar{k}_x(\Delta x/2) + i\bar{k}_y(\Delta y/2)]$

Here we present band-limited reconstructors for hexagonal arrays. Hexagonal geometry may be well suited for adaptive optic systems for large telescopes with hexagonal mirror arrays (e.g., James Webb).¹⁷ Large deformable mirrors used in some laser fusion facilities (National Ignition Facility)¹⁸ also have hexagonal actuator patterns. The number density of lenslets is slightly higher in hexagonal geometry than square. Figure 127.24 shows two possible hexagonal arrays. In Fig. 127.24(a) the unit hexagon is lying on its facet, whereas in Fig. 127.24(b) the unit hexagon is standing on the apex. The circles indicate the measurement points and the \times 's are reconstruction points. In Fig. 127.24(a) geometry, the band-limited derivative calculation for the indicated square array involves first grouping the slopes measured at red- and black-circled positions. Marking them as index 1 and 2, respectively, the DFT's of slopes at the reconstruction points are

$$\widetilde{S}_x = \begin{bmatrix} \widetilde{S}_{1,x} + T_{\text{hex}} \circ \widetilde{S}_{2,x} \\ \widetilde{S}_{1,x} - T_{\text{hex}} \circ \widetilde{S}_{2,x} \end{bmatrix} \equiv \begin{bmatrix} \widetilde{S}_{x,I} \\ \widetilde{S}_{x,II} \end{bmatrix}. \quad (41)$$



E19859JR

Figure 127.24

(a) Prostrate hexagon array; (b) standing hexagon array.

T_{hex} is a matrix whose size is M by N (i.e., the size of either array 1 or array 2) and “ \circ ” denotes entry-wise matrix multiplication. The p th row and q th column element of T_{hex} is

$$T_{\text{hex}}(p,q) = \exp\left[-\frac{\pi i}{M}p - \pi i S(q)\right]. \quad (42)$$

The combined total array is therefore a vertical concatenation of the two matrices. On the other hand, the resulting total matrix for Fig. 127.24(b) geometry is a horizontal concatenation:

$$\begin{aligned}\widetilde{S}_x &= [\widetilde{S}_{1,x} + T_{\text{hex}} \circ \widetilde{S}_{2,x} \quad \widetilde{S}_{1,x} - T_{\text{hex}} \circ \widetilde{S}_{2,x}] \\ &\equiv [\widetilde{S}_{x,\text{I}} \quad \widetilde{S}_{x,\text{II}}].\end{aligned}\quad (43)$$

$$T_{\text{hex}}(p, q) = \exp\left[-\pi i \mathcal{S}(p) - \frac{\pi i}{N} q\right].\quad (44)$$

The same combination rule applies to y-slope measurements.

The above decomposition technique can be inverted such that each subgroup of the hexagonal array can also be expressed as the linear sum of blocks I and II of the rectangular array. This inversion is used only for wavefront points in the algorithm, which is

$$\widetilde{\varphi}_1 = \frac{1}{2}(\widetilde{\varphi}_\text{I} + \widetilde{\varphi}_\text{II}),\quad (45)$$

$$\widetilde{\varphi}_2 = \frac{1}{2}T_{\text{hex}}^* \circ (\widetilde{\varphi}_\text{I} + \widetilde{\varphi}_\text{II}).\quad (46)$$

Using the basic results obtained in **Band-Limited Derivative** (p. 130) and the DFT procedures for the hexagonal arrays in this section, the band-limited reconstruction algorithm for hexagonal slope arrays can be implemented as shown in the flowchart in Fig. 127.25.

Step 1 consists of fitting the slopes over low-order polynomials, e.g., third order, which will significantly reduce non-band-limited components of the wavefront. If the regions of interest are disconnected, the fitting must be performed per each region. Owing to the sum requirement [Eq. (3)], a column and row are appended to the edge of the measured slope matrices (groups 1 and 2 separately), which will satisfy the zero-sum conditions in the x and y directions.

Step 2 initializes the slopes with measured values. Steps 3–8 form a closed loop required for extrapolating slopes outside the non-rectangular region. The iteration is not required if the region is rectangular.

Slopes in groups 1 and 2 are separately Fourier transformed using Eqs. (40)–(43) in Step 3. In Step 4, wavefront matrices corresponding to each block (I or II) are reconstructed in the Fourier domain using the band-limited filter function, which is

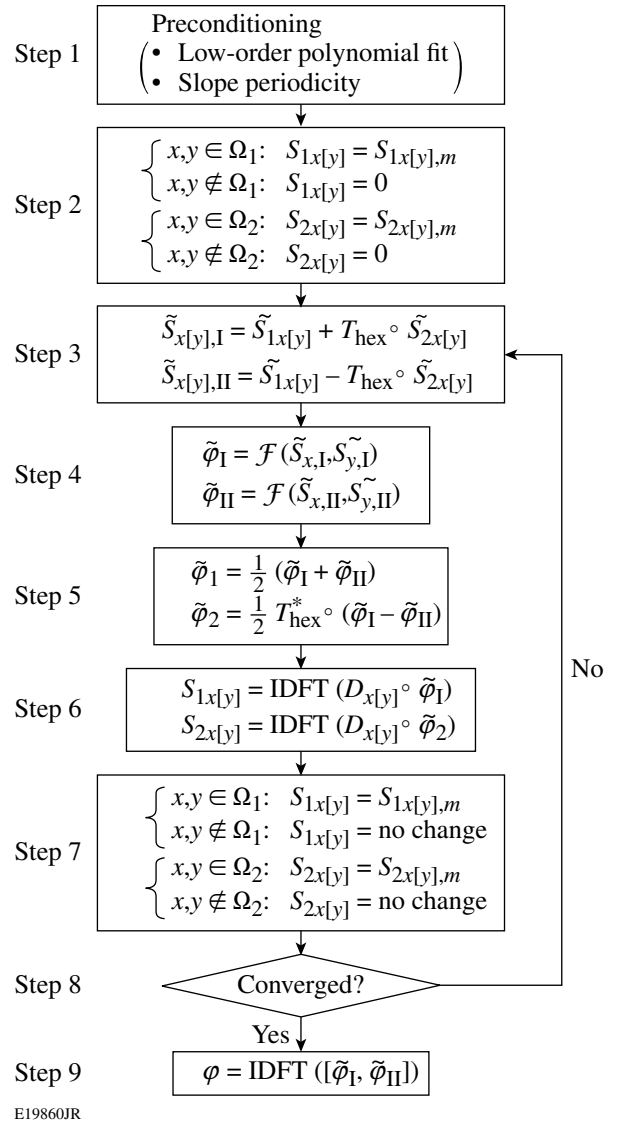


Figure 127.25

Flowchart of band-limited reconstruction for a hexagonal geometry. \mathcal{F} is the band-limited filter function [Eq. (46)]. The “ m ” subscript denotes the measured slopes. IDFT stands for inverse discrete Fourier transform. Ω_1 and Ω_2 are the regions where the slopes’ groups 1 and 2 data exist.

$$\begin{aligned}\mathcal{F} [\widetilde{S}_x(p, q), \widetilde{S}_y(p, q)] \\ = \frac{D_x^*(p, q)\widetilde{S}_x(p, q) + D_y^*(p, q)\widetilde{S}_y(p, q)}{|D_x(p, q)|^2 + |D_y(p, q)|^2},\end{aligned}\quad (47)$$

where the band-limited derivative operators D_x and D_y are defined as

$$D_x(p, q) = \frac{2\pi i}{\Delta x} \mathcal{S}(q), \quad (48)$$

$$D_y(p, q) = \frac{2\pi i}{(2\Delta y)} \mathcal{S}(p), \quad (49)$$

for a prostrate hexagon array and

$$D_x(p, q) = \frac{2\pi i}{(2\Delta x)} \mathcal{S}(q), \quad (50)$$

$$D_y(p, q) = \frac{2\pi i}{\Delta y} \mathcal{S}(p), \quad (51)$$

for a standing hexagon array.

Step 5 creates wavefront groups 1 and 2 by using Eqs. (51) and (52). In Steps 3 and 5, the correct T_{hex} must be used according to its geometry. In Step 6, derivative operators are applied to these temporary wavefront matrices to obtain slopes in groups 1 and 2, respectively. These new slopes are different from the measured slopes. We leave the values external to the boundary untouched while restoring the internal values to the original measured slopes. The difference between the measured slopes and the calculated slopes decreases over the course of iterations. Step 8 determines whether this difference is within tolerance. Once the convergence criterion is met, the wavefront matrices generated in Step 4 ($\overline{\varphi}_I, \overline{\varphi}_{II}$) are combined to form a single matrix by either vertical or horizontal concatenation, depending on the hexagon geometry and inverse Fourier transformed to the spatial domain to produce the final result in Step 9. Small terms in the imaginary part of the solution can be neglected.

The band-limited algorithms shown in Fig. 2 of Ref. 11 and Fig. 127.25 can be used together with a non-band-limited filter function, which enables one to conveniently switch between different algorithms. The reconstruction algorithms proposed here are not limited to a specific boundary shape.

Error Propagation

The wavefront reconstructors have traditionally been characterized with a so-called error propagation curve. This indicates the sensitivity of the noise in the reconstructed phase to the noise in the slopes measurements. Early numerical and theoretical works show that this sensitivity is a logarithmic function of the number of measurement points.^{1,2,15} Simulations confirm this. The noise-propagation coefficient will be calculated using discrete samples and frequency-domain filter functions. We limit the scope to the rectangular area.

Let σ_φ be the root mean square of the reconstructed phase φ . According to the Wiener-Khintchin theorem,

$$\sigma_\varphi^2 = \frac{1}{N_t} \sum \langle \Delta\varphi^2 \rangle = \frac{1}{N_t N^2} \sum \langle |\overline{\Delta\varphi}|^2 \rangle, \quad (52)$$

where $\langle \cdot \rangle$ denotes ensemble average of the quantity inside.

According to linear stochastic system theory, the power spectrum of input and output signals is related by the absolute square of the linear system function. In the case of wavefront reconstruction dictated by the linear response

$$\tilde{\varphi} = \frac{(D_x^* A_x \overline{\mathcal{S}}_x + D_y^* A_y \overline{\mathcal{S}}_y)}{|D_x|^2 + |D_y|^2 + \lambda(|D_{x,\text{reg}}|^2 + |D_{y,\text{reg}}|^2)}, \quad (53)$$

the corresponding stochastic response in power spectrum is

$$\begin{aligned} & \langle |\overline{\Delta\varphi}|^2 \rangle \\ &= \frac{(|D_x A_x \Delta \overline{\mathcal{S}}_x|^2 + |D_y A_y \Delta \overline{\mathcal{S}}_y|^2)}{[|D_x|^2 + |D_y|^2 + \lambda(|D_{x,\text{reg}}|^2 + |D_{y,\text{reg}}|^2)]^2}. \end{aligned} \quad (54)$$

Assuming that $\Delta \overline{\mathcal{S}}_x$ and $\Delta \overline{\mathcal{S}}_y$ are uncorrelated white noise with a variance of $\overline{\sigma}_S^2$ for each, and since $\sigma_S^2 = (1/N) \overline{\sigma}_S^2$, the noise-propagation coefficient is

$$\begin{aligned} \eta &= \frac{\sigma_\varphi^2}{h^2 \sigma_S^2} \\ &= \frac{1}{L^2} \sum_{k_x, k_y} \frac{(|D_x A_x|^2 + |D_y A_y|^2)}{[|D_x|^2 + |D_y|^2 + \lambda(|D_{x,\text{reg}}|^2 + |D_{y,\text{reg}}|^2)]^2}, \end{aligned} \quad (55)$$

where $\sigma_\varphi^2 = (1/N_t) \langle |\overline{\Delta\varphi}|^2 \rangle$, $h = \Delta x = \Delta y$, and L is the aperture size. This result is equivalent to Noll's¹⁹ in the case of band-limited operators.

Table 127.III summarizes finite-difference derivative/averaging operators for four geometries to be used with Eq. (55).

The right-hand side of Eq. (50) is inversely proportional to $|D_{x,0}|^2 + |D_{y,0}|^2$ for band-limited reconstruction and is difficult to visualize in linear scale. We define a “noise-response function (S_N)” with the inverse power dependence removed as follows:

$$S_N = \frac{(|D_{x,0}|^2 + |D_{y,0}|^2)(|D_x A_x|^2 + |D_y A_y|^2)}{\left[|D_x|^2 + |D_y|^2 + \lambda(|D_{x,reg}|^2 + |D_{y,reg}|^2)\right]^2}. \quad (56)$$

It can be shown by the Cauchy–Schwartz inequality that the noise response is always larger than or equal to the absolute frequency response squared,

$$|H|^2 \leq S_N. \quad (57)$$

The inequality [Eq. (52)] shows that the error propagation is intimately related to the frequency response of a reconstructor. The lower bound of η is

$$\sum_{k_x, k_y} \frac{|H|^2}{k_x^2 + k_y^2} \leq \sum_{k_x, k_y} \frac{S_N}{k_x^2 + k_y^2} = \eta. \quad (58)$$

From this, one can expect that the Southwell reconstructor will have the lowest lower bound and the Fried reconstructor the highest. It agrees with the result of Zou.²⁰

The analytic expression for η can be calculated and fit to a logarithmic curve, although the logarithm dependence is only approximate except for the band-limited reconstructors. The result is summarized in the second column of Table 127.IV. Singularity points were excluded in the summation over spatial-

frequency space. The third column shows the simulated η obtained by running actual reconstructors with zero slopes input with Gaussian noise. Two hundred realizations were performed at each N , where N^2 is the number of points. N was varied from 10 to 100 by 10. The logarithm fit over the averaged η is shown in the column. The multiplicative coefficients roughly agree with the analytic ones up to the second decimal point, but the additive constants from simulation are always estimated higher than the calculated ones. The offset is about 0.2771 on average. The discrepancy appears to come from the apparent inconsistency in assuming white noise in the slopes power spectrum and the use of band-limited derivative formalism. For example, the reconstructed wavefront from white spectrum noise always has some amount of low-order polynomial terms, which cannot be represented by Eq. (48). The constant offset 0.2771 therefore can be considered as the ratio of energy conversion from white noise to non-band-limited signals.

The legacy formulas of noise propagation for each reconstructor are also shown in the fourth column of Table 127.IV, quoted from the three authors' original publications.^{1,2,15} The quoted Southwell η is estimated only from the graph in the original paper since no explicit formula was given. Noll's calculation essentially corresponds to the band-limited case. Considering the fact that there is some ambiguity in the determination of the constant offset, at least the multiplicative coefficient of the Fried formula comes close to our analytic result; whereas there

Table 127.III: Summary of frequency-domain equivalents of the associated finite-difference schemes.

Finite-difference scheme	D_x	A_x
Southwell ¹⁴	$\frac{1}{\Delta x}[\exp(i\bar{k}_x \Delta x) - 1]$	$\frac{1}{2}[\exp(i\bar{k}_x \Delta x) + 1]$
Hudgin ²	$\frac{1}{\Delta x}[\exp(i\bar{k}_x \Delta x) - 1]$	1
Fried ¹	$\frac{1}{2\Delta x}[\exp(i\bar{k}_x \Delta x) - 1][\exp(i\bar{k}_y \Delta y) + 1]$	1
Simpson	$\frac{1}{2\Delta x}[\exp(i\bar{k}_x \Delta x) - \exp(-i\bar{k}_x \Delta x)]$	$\frac{1}{6}[\exp(i\bar{k}_x \Delta x) + 4 + \exp(-i\bar{k}_x \Delta x)]$

Table 127.IV: Summary of noise propagation.

Numerical Scheme	Calculated η	Simulated η	Quoted η
Southwell difference	$-0.1211 + 0.1591 \ln N$	$0.1356 + 0.1638 \ln N$	$-0.1237 + 0.3164 \ln N$
Hudgin difference	$0.0485 + 0.1592 \ln N$	$0.3456 + 0.1528 \ln N$	$0.561 + 0.103 \ln N$
Fried difference	$-0.0865 + 0.3202 \ln N$	—	$0.6558 + 0.3206 \ln N$
Band limited	$-0.0285 + 0.1594 \ln N$	$0.2449 + 0.1615 \ln N$	$0.1072 + 0.318 \ln N$
Simpson difference	$0.0314 + 0.1610 \ln N$	$0.3125 + 0.1647 \ln N$	—

is about a factor-of-2 difference in the Southwell and Noll's expression compared with ours. On the other hand, Hudgin's formula does not agree with our results. Fried's formula is based on a comparatively large number of N (≤ 39) compared with Southwell and Hudgin's calculations ($N \leq 20$).

Conclusion

We have presented derivations of band-limited derivative operators in the frequency domain. These are important tools for characterizing and improving the frequency response of wavefront reconstructors over broad bandwidth. Two new wavefront reconstructors were proposed utilizing these tools. The reconstructors were designed to be accurate up to high spatial frequency. The first one is based on the Simpson integration rule. The bandwidth of the frequency response of this reconstructor, after being regularized, is excellent up to 85% of the spatial frequency range. A successive-over-relaxation iterative solver was presented in detail, where the outermost samples are elegantly handled using g flags. The frequency-response behavior of the iterative solver agrees well with the predicted frequency-response curve. The second reconstructor is an extension of the band-limited reconstruction algorithm previously developed; the measurement points are on a hexagonal array instead of a rectangular array. A Fourier-domain iterative algorithm was proposed for two types of hexagonal arrays. As was previously pointed out in Ref. 11, the reconstruction process must be preconditioned with the low-order polynomial fit. The Simpson-rule-based algorithm works purely in the spatial domain; therefore, it is computationally less complex than band-limited algorithms, whereas the latter provides flexibility against any geometry change. Fourier-domain algorithms have a potential of boosting reduction speed with the help of digital-signal processors.

The new wavefront reconstructors are compared with the traditional reconstructors in terms of noise-propagation properties through a generalized noise-propagation expression. The analytically calculated noise-propagation coefficients are consistent with the numerical fit deduced from our own simulations. We did not find, however, universal agreement with the published results.

The broad-bandwidth wavefront reconstructors developed here are used in wavefront-reduction software to characterize focal spots of the OMEGA EP laser beams.¹³ The importance of the band-limited reconstructor was well illustrated in Ref. 21 for a closed-loop wavefront-shaping application. One may also find applications in the study of metrology and atmospheric turbulence.²²

ACKNOWLEDGMENT

This work was supported by the U.S. Department of Energy Office of Inertial Confinement Fusion under Cooperative Agreement No. DE-FC52-08NA28302, the University of Rochester, and the New York State Energy Research and Development Authority. The support of DOE does not constitute an endorsement by DOE of the views expressed in this article.

REFERENCES

1. D. L. Fried, *J. Opt. Soc. Am.* **67**, 370 (1977).
2. R. H. Hudgin, *J. Opt. Soc. Am.* **67**, 375 (1977).
3. K. R. Freischlad and C. L. Koliopoulos, *J. Opt. Soc. Am. A* **3**, 1852 (1986).
4. F. Roddier and C. Roddier, *Appl. Opt.* **30**, 1325 (1991).
5. L. A. Poyneer, D. T. Gavel, and J. M. Brase, *J. Opt. Soc. Am. A* **19**, 2100 (2002).
6. L. A. Poyneer and B. Macintosh, *J. Opt. Soc. Am. A* **21**, 810 (2004).
7. A. Dubra, C. Paterson, and C. Dainty, *Appl. Opt.* **43**, 1108 (2004).
8. C. Elster and I. Weingartner, in *X-Ray Mirrors, Crystals, and Multilayers II*, edited by A. K. Freund *et al.* (SPIE, Bellingham, WA, 2002), Vol. 4782, pp. 12–20.
9. J. Campos *et al.*, *Opt. Lett.* **27**, 1986 (2002).
10. L. Yaroslavsky, A. Moreno, and J. Campos, *Opt. Express* **13**, 2892 (2005).
11. S.-W. Bahk, *Opt. Lett.* **33**, 1321 (2008).
12. M. Servin, D. Malacara, and J. L. Marroquin, *Appl. Opt.* **35**, 4343 (1996).
13. J. Bromage, S.-W. Bahk, D. Irwin, J. Kwiatkowski, A. Pruyne, M. Millecchia, M. Moore, and J. D. Zuegel, *Opt. Express* **16**, 16,561 (2008).
14. R. Marks, II and M. W. Hall, *IEEE Trans. Audio, Speech, Lang. Process.* **29**, 872 (1981).
15. W. H. Southwell, *J. Opt. Soc. Am.* **70**, 998 (1980).
16. D. L. Phillips, *J. ACM* **9**, 84 (1962).
17. See <http://www.jwst.nasa.gov/>.
18. S. E. Winters, J. H. Chung, and S. A. Velinsky, *J. Dyn. Syst. Meas. Contr.* **124**, 297 (2002).
19. R. J. Noll, *J. Opt. Soc. Am.* **68**, 139 (1978).
20. W. Zou and J. P. Rolland, *J. Opt. Soc. Am. A* **23**, 2629 (2006).
21. S.-W. Bahk, E. Fess, B. E. Kruschwitz, and J. D. Zuegel, *Opt. Express* **18**, 9151 (2010).
22. T. W. Nicholls, G. D. Boreman, and J. C. Dainty, *Opt. Lett.* **20**, 2460 (1995).

Time-Resolved Optical Response of All-Oxide, $\text{YBa}_2\text{Cu}_3\text{O}_7/\text{La}_{0.7}\text{Sr}_{0.3}\text{MnO}_3$ Proximitized Bilayers

The interplay between superconductivity (S) and ferromagnetism (F) is one of the most intriguing and challenging fields of research in solid-state physics. The proximity effect at the interface between traditional, both metallic, S and F films has been widely investigated.¹ In comparison, properties of bilayers consisting of high-temperature superconducting cuprates and ferromagnetic manganites are much less understood, despite large research activities and substantial progress in the comprehension of the physics of the involved materials.^{2–4} The superconducting proximity effect at the S/F interface is governed by the short coherence length of the cuprate $\xi_0 \approx v_F/2\Delta$ and by the even shorter coherence length $\xi_m \approx v'_F/2E_b$ in manganites, where v_F and v'_F are the Fermi velocities in the S and F layers, respectively, Δ is the superconducting energy gap, and $E_b \approx 3$ eV is the manganite exchange energy.⁵ At the interface, a layer with a thickness of about ξ_0 within the superconductor is expected to show a depressed superconductivity that, in combination with extremely short ξ_m , suggests that Cooper pairs should not practically penetrate into the F layer. This simple consideration is, however, still subject to debate since an unexpected long-range proximity effect recently reported^{3,6,7} has been ascribed to the spin superconducting triplet-pairing at the F side of the bilayer in the presence of magnetic inhomogeneities or domain walls.^{6,8} Magnetic properties of the S/F interface, on the other hand, are governed by the short-length exchange field and associated to nonconventional ordering of Cu spins,⁴ while longer-range effects depend on the spin-diffusion mechanism.⁹ Finally, the establishment of the equilibrium chemical potential determines a charge transfer,² with screening length of the order of 1 to 2 nm, determining “dead layers” on both the S and F sides.

Cuprate/manganite oxide, nanostructured heterostructures are likely to have a high potential for applications. Beside a constantly growing field of spintronics, our research attention has been devoted to $\text{YBa}_2\text{Cu}_3\text{O}_7/\text{La}_{0.7}\text{Sr}_{0.3}\text{MnO}_3$ (YBCO/LSMO) hybrids as possible, artificially engineered, ultrafast optoelectronics devices.^{10,11} However, nonequilibrium properties of the S/F bilayers are far from being fully characterized

and understood. Time-resolved pump–probe ultrafast optical spectroscopy can provide a great deal of information on the dynamics of such complex structures.¹² In this article, we present the successful fabrication of epitaxial YBCO/LSMO nanobilayers and their subpicosecond pump–probe characterization in a temperature range below and above the superconducting critical temperature T_c .

Our YBCO/LSMO heterostructures were grown by pulsed-laser deposition on (001) SrTiO_3 substrates (with a single TiO_2 termination layer), in an O_2 atmosphere at 0.25-Mbar pressure, for deposition of both the first (YBCO) and the second (LSMO) layers. The growth process was performed at 800°C and was controlled *in situ* by the reflection high-energy electron diffraction (RHEED) method. The RHEED patterns demonstrated very high crystallinity of our bilayer structures at every step of the process.¹⁰ Cooling of the samples included a prolonged exposure to 200 Mbar of O_2 at 500°C, to promote full oxidation of YBCO through the LSMO capping. The resulting nanostructures had excellent structural and transport properties, with $\sim 0.3^\circ$ full-width-at-half-maximum rocking curves and sharp superconducting transition (T_{c0} up to 91.5 K, $\Delta T_c \sim 0.3$ K). From measurements of the conductivity's dependence on temperature, we could deduce that the Curie temperature T_c of LSMO largely exceeded room temperature, concluding that in our experiments, even under optical illumination, the LSMO film always remained in the ferromagnetic state. Our test samples consisted of a plain, 100-nm-thick YBCO film (a reference sample) and a sequence of 100-nm-thick YBCO layers capped with 10 and 35 nm of LSMO, respectively (named LY10 and LY35, respectively). The LSMO thicknesses guaranteed a partially transparent behavior at near-infrared wavelengths since, based on our conductivity data, the optical penetration depth was estimated to be

$$\delta \approx \sqrt{\frac{2\varepsilon_0 c^2}{\sigma_0 \omega}} \approx 100 \text{ nm}$$

at our lowest test temperatures.

The femtosecond pump–probe spectroscopy experiments were performed using a mode-locked Ti:sapphire laser, which produced 100-fs pulses at 810-nm wavelength and a 76-MHz repetition rate. The pump and probe beams were focused onto the sample, down to 30 μm in diameter, and cross polarized to eliminate the coherent artifact caused by the direct interference of the two beams. The pump-to-probe average power ratio was set at 10:1 with the pump power set at the 30-mW level (400 pJ of energy per pulse), in order to minimize optical heating and, simultaneously, ensure a good signal-to-noise ratio. The samples were mounted on a cold finger, inside a temperature-controlled, liquid-helium, continuous-flow optical cryostat, operating down to 4 K.

Typical recorded data of the relative optical-reflectivity change $\Delta R/R$ versus time delay are presented in Fig. 127.26. Figure 127.26(a) shows the $\Delta R/R(t)$ waveforms for the reference 100-nm-thick YBCO film, recorded at different temperatures.

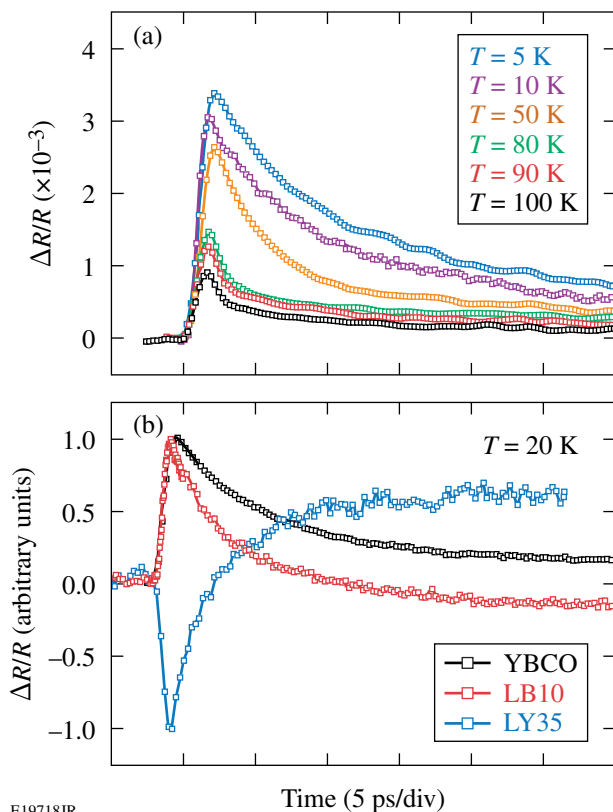
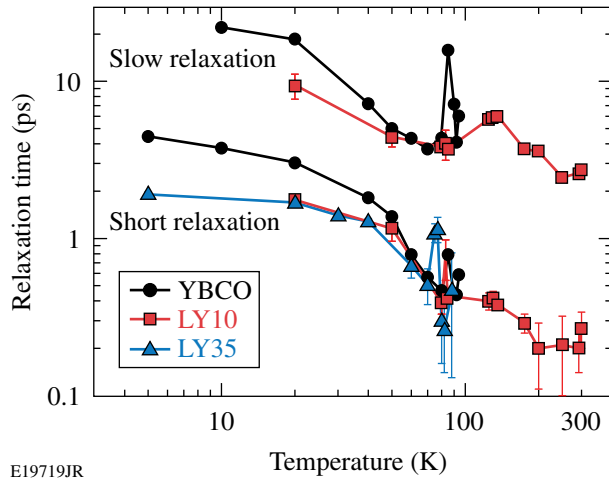


Figure 127.26 (a) The photoresponse $\Delta R/R$ transient versus delay time for a 100-nm-thick YBCO film at different temperatures. (b) The normalized $\Delta R/R$ waveforms versus delay time measured at 20 K for the reference YBCO film and the LY10 and LY35 S/F bilayers.

According to earlier studies on high- T_c materials,¹³ the amplitude of the $\Delta R/R$ signal grows below T_c , while, simultaneously, the recovery becomes progressively slower. This is consistent with other pump–probe studies performed under low-fluence excitations.^{13,14} Contrary to some earlier observations,^{15,16} our data are fitted by a simple linear recombination model, and weak, damped oscillations on top of the exponential decay might, tentatively, be ascribed to displaced excitation of coherent acoustic phonons.^{15,17} Overall, our observations for the pure YBCO film are in agreement with reported data^{14,18–20} and corroborate current interpretation that the slow dynamics below T_c (several tens of picoseconds) cannot be ascribed to the acoustic phonon bottleneck, in contrast with the case of low- T_c superconductors.²¹ In high- T_c materials, recombination of two quasiparticles into a Cooper pair by emission of an acoustic phonon is, in fact, forbidden because the quasiparticle's velocity is faster than the sound velocity²² and the Cooper-pair recombination reflects a complex kinematics involving both nodal and anti-nodal quasiparticles.^{18,19}

The $\Delta R/R$ transients collected at 20 K for two YBCO/LSMO bilayers (LY10 and LY35) and the YBCO reference sample are shown in Fig. 127.26(b). We observe that the thickness of the LSMO overlayer is critically important to the bilayer photoresponse. While the functional dependence of waveform LY10 follows that of the YBCO sample, although with reduced relaxation time, the LY35 curve is very different: it consists of a negative initial peak, followed by an extended relaxation tail, which crosses into the positive values of the $\Delta R/R$ dependence. The negative peak with a time constant ≤ 1 ps can be due to the presence of an additional relaxation mechanism related most likely to localized traps at the S/F interface²³ or multiple reflection from thin heterostructures.

During the course of our research, we have collected dozens of $\Delta R/R$ waveforms for all three samples in the temperature range from 4 K to 300 K, under nominally the same optical pump–probe conditions, and have fitted the data with bi-exponential functions containing two characteristic relaxation times. The latter was justified by the assumption that well above T_c , the system is simply governed by subpicosecond-in-duration, hot-electron cooling in our two materials, of which LSMO has a somewhat slower relaxation time, while below T_c , the fast relaxation process is related to the electron–phonon interaction and the slow one corresponds to the quasi-particle recombination. The results are summarized in Fig. 127.27, where we plot the fast and slow relaxation time dependences on temperature. First we note that below T_c , our YBCO/LSMO bilayers have relaxation times shorter than YBCO, in agreement with the



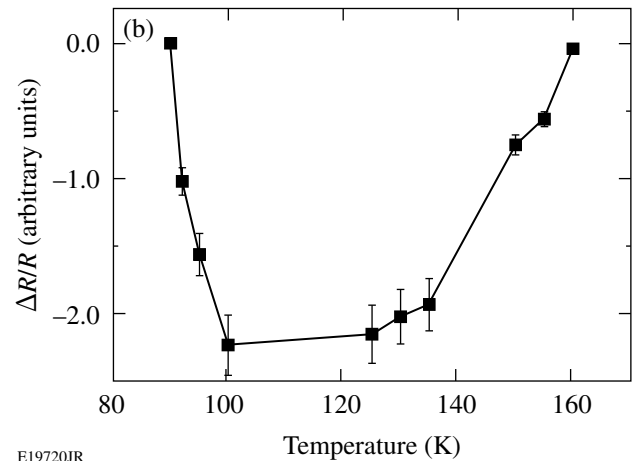
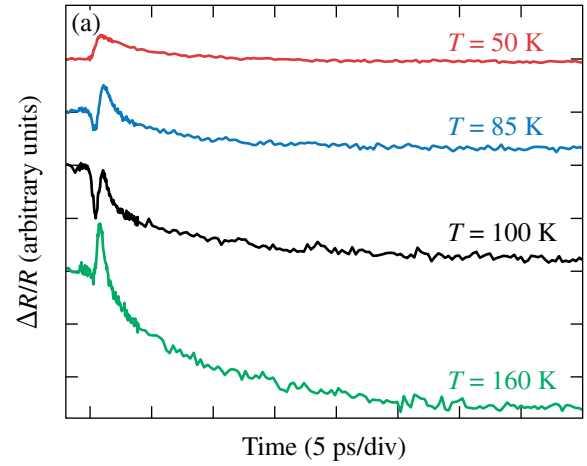
E19719JR

Figure 127.27

The characteristic, both short and slow, relaxation times extracted from the $\Delta R/R(t)$ plots for all our tested samples as a function of temperature.

YBCO/Au/NiCu case.¹⁰ We also observe the presence of sharp peaks in both the fast and slow (YBCO only) relaxation time dependences, which we believe correspond to the occurrence of a superconducting transition within the probed samples, reflecting the change in the quasi-particle dynamics caused by the electronic-specific heat jump.^{21,24} As expected, the T_c peak feature shifts slightly to lower temperatures for the thicker LSMO overlayers but, most interestingly, still remains well visible, contrary to metallic, S/F proximitized bilayers.²⁵ Finally, we note that the characteristic time constant of heat transfer from phonons to the spin-wave gas in LSMO below T_c (Ref. 26) is of the order of 30 ps; consequently, it is essentially out of scale in our measurements.

The active role of the S/F interface results in a clear difference between the dynamics of the bilayers and the mere superposition of behaviors of components films. This is well illustrated by LY10 data shown in Fig. 127.28. Figure 127.28(a) presents examples of the $\Delta R/R$ curves well below T_c , in the vicinity of T_c , and, finally, high above T_c . As mentioned above, in a range of temperature above T_c , we observe a sharp undershoot that precedes the positive $\Delta R/R$ peak. As demonstrated in Fig. 127.28(b), the undershoot quickly increases its magnitude at the superconducting transition, reaching the maximum value at ~ 100 K, remains roughly constant negative in the ~ 100 -K to 140-K range, and finally disappears at ~ 160 K. We stress that no undershoot has ever been observed in either pure LSMO or YBCO films. In our opinion, the undershoot reflects the presence of a few-nm-thick “dead layer” at the S/F interface, with degraded properties. This layer is a result of a charge



E19720JR

Figure 127.28

(a) Examples of photoresponse $\Delta R/R$ transients versus delay time for an LY10 sample at different temperatures. The waveforms are shifted in the y axis for clarity. (b) The magnitude of the $\Delta R/R$ negative peak (undershoot) versus temperature.

transfer from YBCO to LSMO that forms an underdoped YBCO region. The underdoped YBCO (e.g., an oxygen-poor compound) is well known to exhibit a sharp, negative $\Delta R/R$ transient.^{27,28} A similar behavior was also observed for underdoped $\text{Bi}_2\text{Sr}_2\text{CaCu}_2\text{O}_{8+y}$ single crystals.²⁹

The presence of both the depressed-superconductivity layer on the YBCO side and the degraded-magnetic layer on the LSMO side leads to another physical consideration. The quasi particles that are excited in bulk YBCO reach the interface in a characteristic time $d/v_F \approx 100$ fs, comparable with our optical excitation pulse. The quasi-particle injection into the LSMO layer is inhibited because a half metal cannot host free electrons with both spin orientations. Reciprocally, hot electrons from LSMO cannot directly enter the YBCO layer

because they possess only one spin orientation. Within the underdoped YBCO, however, the quasi particles experience a much faster recombination in Cooper pairs since this region acts as an energy trap (suppressed Δ region) that substantially shortens their relaxation process. The concept of excitations being trapped at the boundary between a superconductor and a half metal seems to be quite general and the subject certainly deserves further investigation, both experimental and theoretical. Our early results indicate, however, that this mechanism may efficiently enhance the speed of relaxation of an optically perturbed, nonequilibrium, high- T_c superconductor, capped by the ultrathin F layer.

In conclusion, we investigated the temperature dependence of the nonequilibrium dynamics of YBCO/LSMO nanostructured bilayers in the temperature range from 4 K to room temperature. Experiments have demonstrated the active role of the S/F interface, where the electronic charge transfer from $\text{La}_{0.7}\text{Sr}_{0.3}\text{MnO}_3$ to $\text{YBa}_2\text{Cu}_3\text{O}_7$ determines a thin layer with degraded properties. The LSMO/YBCO bilayers are characterized by quasi-particle relaxation times that are shorter than those of the pure YBCO film, opening a new route to their possible applications in the field of ultrafast superconducting optoelectronics.

ACKNOWLEDGMENT

The authors gratefully acknowledge M. Cuoco for fruitful discussion and D. Pan for assistance in early experiments. The work was partially supported by the European Union under the MAMA project (Napoli, Italy) and by the NSF ECCS under Grant No. 0824075 (University of Rochester, Rochester, NY, USA).

REFERENCES

1. E. A. Demler, G. B. Arnold, and M. R. Beasley, *Phys. Rev. B* **55**, 15174 (1997).
2. S. Yunoki *et al.*, *Phys. Rev. B* **76**, 064532 (2007).
3. V. Peña *et al.*, *Phys. Rev. B* **69**, 224502 (2004).
4. J. Chakhalian *et al.*, *Nat. Phys.* **2**, 244 (2006).
5. J. Y. T. Wei *et al.*, *J. Appl. Phys.* **83**, 7366 (1998).
6. I. Asulin *et al.*, *Phys. Rev. B* **74**, 092501 (2006).
7. T. Holden *et al.*, *Phys. Rev. B* **69**, 064505 (2004).
8. A. F. Volkov, F. S. Bergeret, and K. B. Efetov, *Phys. Rev. Lett.* **90**, 117006 (2003).
9. S. Soltan, J. Albrecht, and H.-U. Habermeier, *Phys. Rev. B* **70**, 144517 (2004).
10. G. P. Pepe, L. Parlato, N. Marrocco, V. Pagliarulo, G. Peluso, A. Barone, F. Tafuri, U. Scotti di Uccio, F. Miletto, M. Radovic, D. Pan, and R. Sobolewski, *Cryogenics* **49**, 660 (2009).
11. N. Marrocco, G. P. Pepe, A. Capretti, L. Parlato, V. Pagliarulo, G. Peluso, A. Barone, R. Cristiano, M. Ejrnaes, A. Casaburi, N. Kashiwazaki, T. Taino, H. Myoren, and R. Sobolewski, *Appl. Phys. Lett.* **97**, 092504 (2010).
12. X. Zou *et al.*, *Appl. Phys. Lett.* **97**, 141910 (2010).
13. M. L. Schneider, S. Rast, M. Onellion, J. Demsar, A. J. Taylor, Y. Glinka, N. H. Tolk, Y. H. Ren, G. Lüpke, A. Xu, Y. Klimov, R. Sobolewski, W. Si, X. H. Zeng, A. Soukiassian, X. X. Xi, M. Abrecht, D. Ariosa, D. Pavuna, A. Krapf, R. Manzke, J. O. Printz, M. S. Williamsen, K. E. Downum, P. Guptaarma, and I. Bozovic, *Eur. Phys. J. B* **36**, 327 (2003).
14. N. Gedik *et al.*, *Science* **300**, 1410 (2003).
15. B. Mansart *et al.*, *J. Mod. Opt.* **57**, 959 (2010).
16. X. Li, Y. Xu, Š. Chromik, V. Štrbík, P. Odier, D. De Barros, and R. Sobolewski, *IEEE Trans. Appl. Supercond.* **15**, 622 (2005).
17. I. Bozovic, M. Schneider, Y. Xu, R. Sobolewski, Y. H. Ren, G. Lüpke, J. Demsar, A. J. Taylor, and M. Onellin, *Phys. Rev. B* **69**, 132503 (2004).
18. P. C. Howell, A. Rosch, and P. J. Hirschfeld, *Phys. Rev. Lett.* **92**, 037003 (2004).
19. C. W. Luo *et al.*, *J. Appl. Phys.* **102**, 033909 (2007).
20. X. Deng *et al.*, *Phys. Rev. B* **77**, 144528 (2008).
21. A. Rothwarf and B. N. Taylor, *Phys. Rev. Lett.* **19**, 27 (1967).
22. B. J. Feenstra *et al.*, *Phys. Rev. Lett.* **79**, 4890 (1997).
23. L. Vasiliu-Doloc *et al.*, *Phys. Rev. Lett.* **83**, 4393 (1999).
24. J. Demsar *et al.*, *Phys. Rev. Lett.* **82**, 4918 (1999).
25. T. Taneda, G. P. Pepe, L. Parlato, A. A. Golubov, and R. Sobolewski, *Phys. Rev. B* **75**, 174507 (2007).
26. R. D. Averitt and A. J. Taylor, *J. Phys. (USSR)* **14**, R1357 (2002).
27. L. Shi, T. Gong, X. Weng, Y. Kostoulas, R. Sobolewski, and P. M. Fauchet, *Appl. Phys. Lett.* **64**, 1150 (1994).
28. K. H. Wu *et al.*, *Chin. J. Phys.* **38**, 279 (2000).
29. Y. H. Liu *et al.*, *Phys. Rev. Lett.* **101**, 137003 (2008).

Publications and Conference Presentations

Publications

- T. R. Boehly, V. N. Goncharov, W. Seka, M. A. Barrios, P. M. Celliers, D. G. Hicks, G. W. Collins, S. X. Hu, J. A. Marozas, and D. D. Meyerhofer, "Velocity and Timing of Multiple Spherically Converging Shock Waves in Deuterium," *Phys. Rev. Lett.* **106**, 195005 (2011).
- J. Bromage, J. M. Fini, C. Dorrer, and J. D. Zuegel, "Characterization and Optimization of Yb-Doped Photonic-Crystal Fiber Rod Amplifiers Using Spatially Resolved Spectral Interferometry," *Appl. Opt.* **50**, 2001 (2011).
- D. E. Fratanduono, T. R. Boehly, M. A. Barrios, D. D. Meyerhofer, J. H. Eggert, R. F. Smith, D. G. Hicks, P. M. Celliers, D. G. Braun, and G. W. Collins, "Refractive Index of Lithium Fluoride Ramp Compressed to 800 GPa," *J. Appl. Phys.* **109**, 123521 (2011).
- M. C. Ghilea, D. D. Meyerhofer, and T. C. Sangster, "Neutron-Induced Nucleation Inside Bubble Chambers Using Freon 115 as the Active Medium," *Nucl. Instrum. Methods Phys. Res. A* **648**, 210 (2011).
- S. X. Hu, "Attosecond Timing the Ultrafast Charge-Transfer Process in Atomic Collisions," *Phys. Rev. A* **83**, 041401(R) (2011).
- G. Li, R. Yan, C. Ren, J. Tonge, and W. B. Mori, "Three-Dimensional Particle-in-Cell Simulations of Laser Channeling in Fast Ignition," *Phys. Plasmas* **18**, 042703 (2011).
- D. D. Meyerhofer, R. L. McCrory, R. Betti, T. R. Boehly, D. T. Casey, T. J. B. Collins, R. S. Craxton, J. A. Delettrez, D. H. Edgell, R. Epstein, K. A. Fletcher, J. A. Frenje, V. Yu. Glebov, V. N. Goncharov, D. R. Harding, S. X. Hu, I. V. Igumenshchev, J. P. Knauer, C. K. Li, J. A. Marozas, F. J. Marshall, P. W. McKenty, P. M. Nilson, S. P. Padalino, R. D. Petrasso, P. B. Radha, S. P. Regan, T. C. Sangster, F. H. Séguin, W. Seka, R. W. Short, D. Shvarts, S. Skupsky, J. M. Soures, C. Stoeckl, W. Theobald, and B. Yaakobi, "High-Performance Inertial Confinement Fusion Target Implosions on OMEGA," *Nucl. Fusion* **51**, 053010 (2011).
- P. M. Nilson, A. A. Solodov, J. F. Myatt, W. Theobald, P. A. Jaanimagi, L. Gao, C. Stoeckl, R. S. Craxton, J. A. Delettrez, B. Yaakobi, J. D. Zuegel, B. E. Kruschwitz, C. Dorrer, J. H. Kelly, K. U. Akli, P. K. Patel, A. J. Mackinnon, R. Betti, T. C. Sangster, and D. D. Meyerhofer, "Scaling Hot-Electron Generation to Long-Pulse, High-Intensity Laser-Solid Interactions," *Phys. Plasmas* **18**, 056703 (2011).
- P. M. Nilson, W. Theobald, C. Mileham, C. Stoeckl, J. F. Myatt, J. A. Delettrez, J. MacFarlane, I. A. Begishev, J. D. Zuegel, R. Betti, T. C. Sangster, and D. D. Meyerhofer, "Target-Heating Effects on the $K_{\alpha_{1,2}}$ -Emission Spectrum from Solid Targets Heated by Laser-Generated Hot Electrons," *Phys. Plasmas* **18**, 042702 (2011).
- A. V. Okishev, "Characterization of Highly Stable Mid-IR, GaSb-Based Laser Diodes," *Opt. Express* **19**, 9863 (2011).
- S. Papernov, A. Tait, W. Bittle, A. W. Schmid, J. B. Oliver, and P. Kupinski, "Near-Ultraviolet Absorption and Nanosecond-Pulse-Laser Damage in HfO₂ Monolayers Studied by Submicrometer-Resolution Photothermal Heterodyne Imaging and Atomic Force Microscopy," *J. Appl. Phys.* **109**, 113106 (2011).
- P. B. Radha, R. Betti, T. R. Boehly, J. A. Delettrez, D. H. Edgell, V. N. Goncharov, I. V. Igumenshchev, J. P. Knauer, J. A. Marozas, F. J. Marshall, R. L. McCrory, D. D. Meyerhofer, S. P. Regan, T. C. Sangster, W. Seka, S. Skupsky, A. A. Solodov, C. Stoeckl, W. Theobald, J. A. Frenje, D. T. Casey, C. K. Li, and R. D. Petrasso, "Inertial Confinement Fusion Using the OMEGA Laser System," *IEEE Trans. Plasma Sci.* **39**, 1007 (2011).
- S. P. Regan, H. Sawada, V. N. Goncharov, D. Li, P. B. Radha, R. Epstein, J. A. Delettrez, S. X. Hu, V. A. Smalyuk, B. Yaakobi, T. R. Boehly, T. C. Sangster, D. D. Meyerhofer, R. L. McCrory, and R. C. Mancini, "Spectroscopic Observa-

tions of Fermi-Degenerate Aluminum Compressed and Heated to Four Times Solid Density and 20 eV,” *High Energy Density Phys.* **7**, 259 (2011).

W. Theobald, A. A. Solodov, C. Stoeckl, K. S. Anderson, R. Betti, T. R. Boehly, R. S. Craxton, J. A. Delettrez, C. Dorrer, J. A.

Frenje, V. Yu. Glebov, H. Habara, K. A. Tanaka, J. P. Knauer, F. J. Marshall, K. L. Marshall, D. D. Meyerhofer, P. M. Nilson, P. K. Patel, H. Chen, T. C. Sangster, W. Seka, N. Sinenian, T. Ma, F. N. Beg, E. Giraldez, and R. B. Stephens, “Initial Cone-in-Shell Fast-Ignition Experiments on OMEGA,” *Phys. Plasmas* **18**, 056305 (2011).

Forthcoming Publications

J. Bromage, J. Rothhardt, S. Hädrich, C. Dorrer, C. Jocher, S. Demmler, J. Limpert, A. Tünnermann, and J. D. Zuegel, “Analysis and Suppression of Parasitic Processes in Noncollinear Optical Parametric Amplifiers,” to be published in *Optics Express*.

P. Y. Chang, G. Fiksel, M. Hohenberger, J. P. Knauer, R. Betti, F. J. Marshall, D. D. Meyerhofer, F. H. Séguin, and R. D. Petrasso, “Fusion Yield Enhancement in Magnetized Laser-Driven Implosions,” to be published in *Physical Review Letters*.

E. D. Głowacki, K. L. Marshall, C. W. Tang, and N. S. Sariciftci, “Doping of Organic Semiconductors Induced by Lithium Fluoride/Aluminum Electrodes Studied by Electron Spin Resonance and Infrared Reflection-Absorption Spectroscopy,” to be published in *Applied Physics Letters*.

I. Íñiguez-de-la-Torre, S. Purohit, V. Kaushal, M. Margala, M. Gong, R. Sobolewski, D. Wolpert, P. Ampadu, T. González, and J. Mateos, “Exploring Digital Logic Design Using Nanometer-Scale Devices Through Monte Carlo Simulations,” to be published in *IEEE Transactions on Nanotechnology*.

C. Miao, R. Shen, M. Wang, S. N. Shafrir, H. Yang, and S. D. Jacobs, “Rheological Study of Aqueous Magnetorheological Fluid Using Dual Oxide Coated Carbonyl Iron Particles,” to be published in the *Journal of the American Ceramic Society*.

M. Mikulics, P. Kordoš, D. Gregušová, R. Adam, M. Kočan, S. Wu, J. Zhang, R. Sobolewski, D. Grützmacher, and M. Marso, “Monolithic Integration of Ultrafast Photodetector and MESFET in the GaN Material System,” to be published in *IEEE Photonics Technology Letters*.

R. Nora and R. Betti, “One-Dimensional Planar Hydrodynamic Theory of Shock Ignition,” to be published in *Physics of Plasmas*.

B. B. Pollock, C. E. Clayton, J. E. Ralph, F. Albert, A. Davidson, L. Divol, C. Filip, S. H. Glenzer, K. Herpoldt, W. Lu, K. Marsh, J. Meinecke, W. B. Mori, A. Pak, T. C. Rensink, J. S. Ross, J. Shaw, G. R. Tynan, C. Joshi, and D. H. Froula, “Demonstration of a Narrow Energy Spread, ~0.5 GeV Electron Beam from a Two-Stage Laser Wakefield Accelerator,” to be published in *Physical Review Letters*.

B. Xu and S. X. Hu, “Effects of Electron-Ion Temperature Equilibration on Inertial Confinement Fusion Implosions,” to be published in *Physical Review E*.

J.-H. Yang and R. S. Craxton, “An Empirical Model of Collective Electrostatic Effects for Laser-Beam Channeling in Long-Scale-Length Relativistic Plasmas,” to be published in *Physics of Plasmas*.

Conference Presentations

The following presentations were made at the Omega Laser Facility Users Group Workshop, Rochester, NY, 27–29 April 2011:

D. H. Froula, M. Bedzyk, R. Boni, R. Brown, R. S. Craxton, T. Duffy, F. Ehrne, S. Ivancic, R. Jungquist, J. Puth, W. Seka, M. J. Shoup, III, C. Stoeckl, W. Theobald, D. Weiner, and N. Kugland “The OMEGA EP 4ω Probe and Associated Plasma Diagnostics.”

V. N. Goncharov, “Tuning Low-Adiabatic Cryogenic Implosions on OMEGA.”

B. E. Kruschwitz, “Static Wavefront Correction on OMEGA EP.”

P. W. McKenty, K. S. Anderson, R. Nora, C. Stoeckl, W. Theobald, J. Bates, A. Schmitt, M. Lafon, X. Ribeyre, G. Schurtz, S. Weber,

V. Tykhonchuk, S. Atzeni, J. Perkins, and O. Klimo, "Overview of the Current Status of Shock Ignition."

S. F. B. Morse, "Omega Facility Update: Progress on OLUG Recommendations."

G. Pien, "OMEGA Experimental Operations 2011 OLUG Status Report."

The following presentations were made at CLEO 2011, Baltimore, MD, 1–6 May 2011:

C. Dorrer, "Characterization of a High-Contrast Front-End Prototype for the Omega EP Laser Facility."

C. Dorrer, A. Consentino, and D. Irwin, "Direct Estimation of the Intensity Contrast of High-Energy Laser Pulses."

A. V. Okishev, "A Highly Efficient Diode-Pumped Pulsed Laser Based on Room-Temperature Yb:YAG Ceramics."

R. Xin and J. D. Zuegel, "Amplification to the Period-Doubling Limit in an All-Fiber Regenerative Amplifier for High-Intensity Laser Systems."

The following presentations were made at Siemens PLM Connection, Las Vegas, NV, 2–5 May 2011:

C. Robillard, "The Engineer's Notebook."

T. Smith, "TDM to Teamcenter Meta Data Migration Strategy."

The following presentations were made at the Third International Conference on High Energy Density Physics, Lisbon, Portugal, 17–20 May 2011:

T. R. Boehly, "The Velocity and Timing of Multiple Spherically Converging Shock Waves in Liquid Deuterium."

G. Fiksel, P.-Y. Chang, M. Hohenberger, J. P. Knauer, R. Betti, F. J. Marshall, D. D. Meyerhofer, F. H. Séguin, and R. D. Petrasso, "Fusion-Yield Enhancement in Magnetized Laser-Driven Implosions."

S. P. Regan, R. Epstein, B. Hammel, L. J. Suter, J. Ralph, H. Scott, M. A. Barrios, D. K. Bradley, D. A. Callahan, G. W. Collins, S. Dixit, M. J. Edwards, D. R. Farley, S. H. Glenzer, I. E. Golovkin, S. W. Haan, A. Hamza, D. G. Hicks, N. Izumi, J. D. Kilkenny, J. L. Kline, G. A. Kyrala, O. L. Landen, T. Ma, J. J. MacFarlane, R. C. Mancini, R. L. McCrory, N. B. Meezan, D. D. Meyerhofer, A. Nikroo, K. J. Peterson, T. C. Sangster, P. Springer, and R. P. J. Town, "National Ignition Facility (NIF) Implosions: Hydrodynamic Mixing Experiments."

The following presentations were made at the NAS/NAE Committee on the Prospects for IFE Systems, Rochester, NY, 17 June 2011:

V. N. Goncharov, "Modeling of Cryogenic Implosions on OMEGA is Approaching Precision Required for Ignition."

T. J. Kessler, "Diffractive Optics Technology for ICF."

R. L. McCrory, "Laser-Driven Inertial Fusion Energy: Direct-Drive Targets Overview."

J. B. Oliver and A. L. Rigatti, "High-Damage Threshold Coating for ICF Laser Applications."

J. M. Soures, "The Omega Facility is Operated as a User Facility and has Produced the World's Largest ICF Physics and High-Energy-Density-Science Database."

W. Theobald, "Shock-Ignition and Fast-Ignition Research at LLE."

J. D. Zuegel, "New Laser Technologies for OMEGA EP."

The following presentations were made at the 41st Annual Anomalous Absorption Conference, San Diego, CA, 19–24 June 2011:

S. F. DuBois, D. A. Russell, H. X. Vu, and J. F. Myatt, "Strong Langmuir Turbulence in the Nonlinear Saturation of Parametric Instabilities Driven by Coherent Electromagnetic Waves."

D. H. Edgell, I. V. Igumenshchev, W. Seka, J. F. Myatt, V. N. Goncharov, R. S. Craxton, J. A. Delettrez, A. V. Maximov, R. W. Short, P. W. McKenty, "Crossed-Beam Energy Transfer in Polar Direct-Drive Implosions."

D. H. Froula, D. H. Edgell, I. V. Igumenshchev, P. B. Radha, and V. N. Goncharov, "Thomson Scattering Study of the Coronal Plasma Conditions in Direct-Drive Implosions."

S. X. Hu, D. H. Edgell, D. H. Froula, V. N. Goncharov, W. Seka, S. Skupsky, and B. Yaakobi, "Simulations and Analyses of Long-Scale-Length Plasma Experiments on the Omega EP Laser Facility."

A. V. Maximov, J. F. Myatt, R. W. Short, I. V. Igumenshchev, D. H. Edgell, and W. Seka, "Modeling of Energy Transfer Between Spatially Incoherent Crossing Laser Beams."

J. F. Myatt, J. Zhang, A. V. Maximov, R. W. Short, D. F. DuBois, D. A. Russell, and H. X. Vu, "Evaluation of a Quasilinear Model for the Two-Plasmon-Decay Instability in Inhomogeneous Plasmas."

W. Seka, I. V. Igumenshchev, D. H. Froula, D. H. Edgell, J. F. Myatt, V. N. Goncharov, R. W. Short, and A. V. Maximov, "Reducing the Cross-Beam Energy Transfer in Direct-Drive Implosion Targets Through Laser-Irradiation Control."

R. W. Short and J. F. Myatt, "Convective Multibeam Two-Plasmon Decay for Beam Configurations Relevant to Polar Direct Drive."

A. A. Solodov, R. Betti, K. S. Anderson, J. F. Myatt, W. Theobald, and C. Stoeckl, "Controlling the Divergence of Laser-Generated Fast Electrons Through Resistivity Gradients in Fast-Ignition Targets."

H. X. Vu, D. F. DuBois, J. F. Myatt, and D. A. Russell, "Langmuir Turbulence and Suprathermal Electron Production from the Two-Plasmon Decay Instability Driven by Crossed Laser Beams in an Inhomogeneous Plasma."

R. Yan, A. V. Maximov, C. Ren, and F. S. Tsung, "Energetic Electron Generation in Two-Plasmon-Decay Instabilities in Direct-Drive Inertial Confinement Fusion."

J. P. Knauer, V. Yu. Glebov, C. Stoeckl, T. C. Sangster, D. D. Meyerhofer, J. A. Caggiano, M. J. Moran, R. Hatarik, J. M. McNaney, S. Friedrich, E. J. Bond, M. J. Eckart, S. J. Padalino, and J. D. Kilkenny, "Neutron Time-of-Flight Measurements on the National Ignition Facility," 38th IEEE International Conference on Plasma Science, Chicago, IL, 26–30 June 2011.

T. R. Boehly, V. N. Goncharov, M. A. Barrios, D. E. Fratanduono, S. X. Hu, T. J. B. Collins, J. A. Marozas, T. C. Sangster, D. D. Meyerhofer, P. M. Celliers, H. F. Robey, D. G. Hicks, and G. W. Collins, "Shock-Timing Measurements in ICF Targets Filled with Cryogenic Deuterium," 2011 APS Shock Compression of Condensed Matter, Chicago, IL, 26 June–1 July 2011.

